Nanoscale Horizons

REVIEW

View Article Online
View Journal | View Issue

Cite this: *Nanoscale Horiz.*, 2025, **10**, 512

Mechanical properties of two-dimensional material-based thin films: a comprehensive review

Abdallah Kamal, [ac] Baosong Li,[bc] Abdullah Solayman,[d] Shaohong Luo, [e] Ian Kinloch, [f] Lianxi Zheng[ac] and Kin Liao ⋆[bc]

Received 24th August 2024,
Accepted 26th November 2024

DOI: 10.1039/d4nh00425f

rsc.li/nanoscale-horizons

Two-dimensional (2D) materials are materials with a thickness of one or a few atoms with intriguing electrical, chemical, optical, electrochemical, and mechanical properties. Therefore, they are deemed candidates for ubiquitous engineering applications. Films and three-dimensional (3D) structures made from 2D materials introduce a distinct assembly structure that imparts the inherent properties of pristine 2D materials on a macroscopic scale. Acquiring the adequate strength and toughness of 2D material structures is of great interest due to their high demand for numerous industrial applications. This work presents a comprehensive review of the mechanical properties and deformation behavior of robust films composed of 2D materials that help them to attain other extraordinary properties. Moreover, the various key factors affecting the mechanical performance of such thin films, such as the lateral size of nanoflakes, fabrication technique of the film, thickness of the film, post-processing, and strain rate, are elucidated.

1. Introduction

Freestanding film-like materials play a crucial role in our technological society. They have been exploited in a myriad of applications, such as protective or adhesive layers, components of batteries[1] or supercapacitors,[2] optoelectronic components,[3] chemical filters,[4] and molecular storage.[5,6] As 2D materials are expanding toward practicality, it is vital to consider their infield performances from the perspective of fundamental properties, such as fracture behavior.[7] That would be a beneficial key for predicting the lifespan and establishing the permitted range of applied loads. Furthermore, understanding the basic prerequisites, including structural integrity and mechanical properties, of such 2D materials in various assembly forms is crucial to ensure their reliability. Recently, there has been a growing focus on developing 2D material-based structures with favorable mechanical properties, exceptional flexibility, and multifunctionality. This attention is particularly driven by the aspiration to develop advanced portable and wearable electronic devices.[8] However, certain persistent challenges remain, including the issue of substantial restacking within the system and the need for robust interfaces among individual nanosheets, necessitating further resolution.

2D materials have an atomic thickness. These materials stand out in terms of mechanical, optical, electrical, chemical, and thermal properties.[9] Accordingly, 2D materials have become an integral part of today's technological applications.[10,11] Among various types of 2D materials, graphene, graphene oxide (GO), hBN, and MXenes have attracted significant attention. Thus, understanding the fracture behavior of these materials is crucial to gauge their performance in applications across many fields. The mechanical properties of various 2D material monolayers have been studied.[12,13] Although there are several such investigations on graphene and GO,[14,15] only few studies on the mechanical behavior of MXenes and other 2D materials exist.[16]

To date, most 2D materials are utilized as nanofillers to enhance the electrical and mechanical properties of polymeric nanocomposites (PNC), in which limited filler content (usually less than 10 wt%) is used.[17,18] Although this low filler content can endow the polymeric matrix with superior properties, it restricts exploiting the full capacity of exceptional properties of pristine 2D materials. The former may be orders of magnitudes inferior to the properties of the latter.[19] As a result, this entails the production of composites in which 2D material fillers can be added in higher content to act as a matrix or even devoid of any other additions.[20] This can be achieved by ordered

[a] *Department of Mechanical and Nuclear Engineering, Khalifa University of Science and Technology, 127788, Abu Dhabi, United Arab Emirates*
[b] *Aerospace Engineering, Khalifa University of Science and Technology, 127788, Abu Dhabi, United Arab Emirates. E-mail: kin.liao@ku.ac.ae*
[c] *Research & Innovation Center for Graphene and 2D Materials (RIC-2D), 127788, Abu Dhabi, United Arab Emirates*
[d] *Advanced Research and Innovation Center, 127788, Abu Dhabi, United Arab Emirates*
[e] *Department of Biomedical Engineering, Khalifa University of Science and Technology, 127788, Abu Dhabi, United Arab Emirates*
[f] *Henry Royce Institute, National Graphene Institute and Department of Materials, University of Manchester, Manchester, M13 9PL, UK*

assembly of nanoscale building blocks into macroscopic structures, like films or fibers.[21,22]

The extraordinary functionalities of biological structures have perpetually motivated researchers to create a diverse range of innovative nanoarchitectures inspired by nature. This innovation, in conjunction with recent progress in materials science, has greatly facilitated the development of such bio-inspired and biomimetic nanostructures, producing enhanced properties and versatile multifunctionality.[23–26] Fragility has been one of the primary restrictions for the practical application of films composed of pristine 2D materials, and this deficiency may be overcome by borrowing from nature's intricate design. For instance, the outstanding mechanical properties of nacre have inspired researchers to assemble 2D material nanosheets into high-performance, freestanding films.[20] The intrinsic factors considered for well-designed, nacre-inspired interface architecture are the intense interfacial bonding and uniform alignment of 2D flakes.[27–29] The controlled orientation of the nanosheet can be aligned either by utilizing external force or interfacial bonding.[30,31]

Due to the outstanding mechanical properties and flexibility of films made of 2D materials,[32] it has magnificent potential in several applications.[33,34] Therefore, it is essential to understand the fracture mechanism of these films. Titanium carbides ($Ti_3C_2T_x$) are one member of the MXenes family that can be assembled to produce films that possess outstanding properties.[35,36] In addition to the hydrophilicity of $Ti_3C_2T_x$, it can be fabricated with a large aspect ratio.[37] Similarly, GO exhibits high solubility and processability. Consequently, both GO and $Ti_3C_2T_x$ nanosheets can simply be assembled to form freestanding films with high packing densities *via* straightforward fabrication approaches, such as vacuum-assisted filtration (VAF), casting, wet spinning, and spray-coating.[38–42] Synthesis and preparation stages of nanosheets are critical in influencing the mechanical properties of 2D material films. For instance, it has been noted that ultrasonication of nanosheets can affect their size, which consequently influences their mechanical properties.[43] Additionally, fabrication techniques, metal impurities, and water content have been proven to influence the acquired mechanical properties of such films.[44] Here, we provide a comprehensive review of the mechanical properties of freestanding films composed of 2D materials. Moreover, various parameters, such as the synthesis approach, fabrication technique of the film, flake's size, post-processing, and the applied strain rate, impacting the mechanical performance of such structures are highlighted and discussed.

2. Mechanical properties and fracture behavior of 2D material monolayers

2D materials, substances that are characterized by a planar structure with a few atomic layer thicknesses, are endowed with exceptional length-to-thickness ratios. The diversity and eminent properties of such planar atomic structures introduce promising solutions for the recent and upcoming technological challenges.[45–47] Accordingly, they are emerging as an integral part of many technological applications.[48] Since the first successful exfoliation of graphene in 2004,[49] 2D material family has expanded rapidly to include several kinds of materials.[50,51] To date, there have been more than 2000 types of 2D materials that can be exfoliated,[52] including graphene,[53] transition metals carbide and nitrides (MXenes),[14,54] hexagonal boron nitride (hBN),[55] transition metal dichalcogenides (TMDs),[56,57] metal–organic frameworks (MOFs),[58] covalent organic frameworks,[59] layered double hydroxides,[60] metal oxides,[61] germanane,[62] silicene,[63] stanine,[64] plumbene,[65] and black phosphorus (BP),[66,67] as illustrated in Fig. 1a. In addition to those currently known, it is anticipated that various bulk precursors can be chemically exfoliated to acquire more 2D materials.[68,69]

Understanding the mechanical properties of macroscopic structures made of 2D materials arises by grasping the fundamental-level performance of 2D material monolayers. The atomistic thinness of such materials allows them to attain superior in-plane strength.[71] Accordingly, it is significant to measure and analyze the mechanical performance and the fracture behavior of freestanding 2D nanosheets in the absence of any underlying materials.[72] Initially, due to the inherent thinness and the sophisticated *in situ* testing technique for thin materials, researchers relied on molecular dynamic (MD) simulation to understand the mechanical and fracture behavior of 2D materials.[73–75] However, various *in situ* approaches managed to investigate experimentally the mechanical properties and fracture behavior of 2D monolayers and a few layers under various loading conditions. These techniques include nanoindentation,[76] micro electrical mechanical system (MEMS) chip-based tensile testing, and manipulator-based methods.[76] Nanoindentation test *via* atomic force microscope (AFM) is the most employed technique for measuring the elastic properties of such materials. It was demonstrated from previous studies[77–81] that graphene and hBN exhibit the highest Young's modulus and fracture strength among all other 2D materials, as illustrated in Fig. 1b and c. The mechanical properties of 2D materials *via* various approaches were discussed in detail by Wang *et al.*[70] Table 1 presents the mechanical properties of the various 2D material monolayers. The observation of the deformation and the measurements of the mechanical test of 2D materials show that both tensile strength and Young's modulus are sensitive to the number of layers.[79,82] The cracks are initiated at defect sites with high levels of atomic defects, such as vacancies, and propagate within the layer with a higher density of defects.[83]

3. Mechanical properties of 2D materials' films

Evaluating the mechanical properties of thin films composed of 2D materials of a manageable size is of interest in assessing their performance in tangible applications. Principally, the mechanical properties, including the strength, stiffness, toughness, and elongation of freestanding 2D material films, are

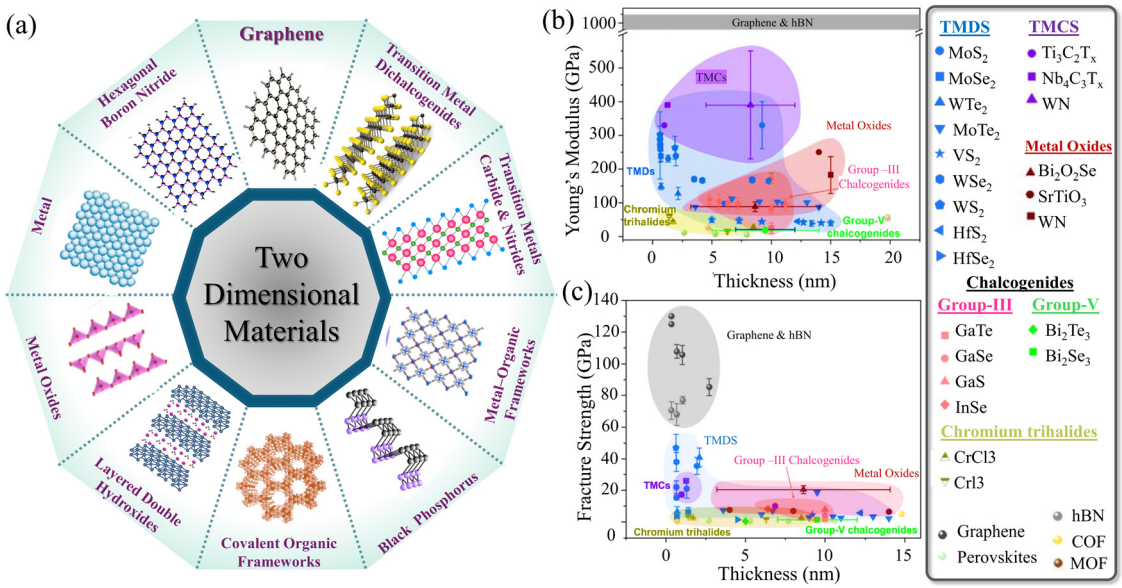

Fig. 1 (a) Schematic of different types of typical 2D nanomaterials.[48,53,55,57–61,67] (b) In-plane Young's modulus, and (c) in-plane fracture strength of various 2D materials. Reproduced with permission.[70] Copyrights © 2023, IOPSCIENCE.

Table 1 Mechanical properties of various 2D material monolayers

2D material	Technique	Young's modulus (GPa)	Tensile strength (GPa)	Strain	Ref.
Graphene	Nanoindentation	1026 ± 22	125	—	78
Graphene	Nanoindentation	1000 ± 100	130 ± 10	0.25	81
Graphene	Nanoindentation	~1000	130	—	84
Graphene	Nanoindentation	997	111	—	85
Graphene	MEMS tensile test	920	~50–60	~6%	86
Graphene	Nanoindentation	1120	—	—	87
Graphene	Nanoindentation	890	—	—	88
Graphene	Nanoindentation	500	30	—	89
rGO	Nanoindentation	250	—	—	80
GO	MEMS tensile test	204 ± 7	12 ± 4	5 ± 0.2%	90
GO	Nanoindentation	207.6 ± 23.4	—	—	79
$Ti_3C_2T_x$	Nanoindentation	330	17.3 ± 1.6	—	16
$Ti_3C_2T_x$	Push-to-pull nanomechanical	484 ± 13	~15.4	~3.2	91
$Nb_4C_3T_x$	Nanoindentation	390	26 ± 1.6	—	92
MoS_2	Nanoindentation	270 ± 100	22 ± 4	—	77
MoS_2	Nanoindentation	264 ± 18	—	—	93
MoS_2	Nanoindentation	330 ± 70	—	—	94
MoS_2	Nanoindentation	300 ± 70	—	—	95
hBN	Nanoindentation	865 ± 73	70.5 ± 5.5	12.5 ± 3%	78
hBN	MEMS tensile test	439.8 ± 77.3	7.9 ± 2.5	—	96
hBN	Nanoindentation	1160	37	0.35%	97
hBN	Nanoindentation	220–255 N m^{-1}	8.8 N m^{-1}	—	98
WSe_2	Nanoindentation	170.3 ± 6.7	~12.4	—	99
WSe_2	Nanoindentation	258.6 ± 38.3	38 ± 6	19.7 ± 4.3%	100
WS_2	Nanoindentation	272 ± 18	—	—	93
WS_2	Nanoindentation	302.4 ± 24.1	47 ± 8.6	19.8 ± 4.3%	100
WTe_2	Nanoindentation	149.1 ± 9.4	6.4 ± 3.3	4.4 ± 2.7%	100
Bi_2Se_3	Nanoindentation	20.7 ± 4.0	1.278 ± 0.29	4–8.3%	101
Bi_2Te_3	Nanoindentation	11.7–25.7	—	—	102
BP	First-principles calculations	106.4	>25	0.11	103
Mica	Nanoindentation	190	—	—	104

attributed to the interlocking tile-like microstructure formed by the constituent nanoflakes throughout the macroscopic film. The alignment and the interlayer characteristics (bonding and cross-linking) between the adjacent nanoflakes are the key factors impacting the overall mechanical performance of these films.[27,105] Thus, the deformation behavior of 2D material films comprises most likely three stages (R_1, R_2, and R_3), as illustrated in Fig. 2a. These stages involve straightening, skin failure, and pull-out and slippage stages. It is obvious that the straightening stage (R_1) is small in terms of the range of strain. During this

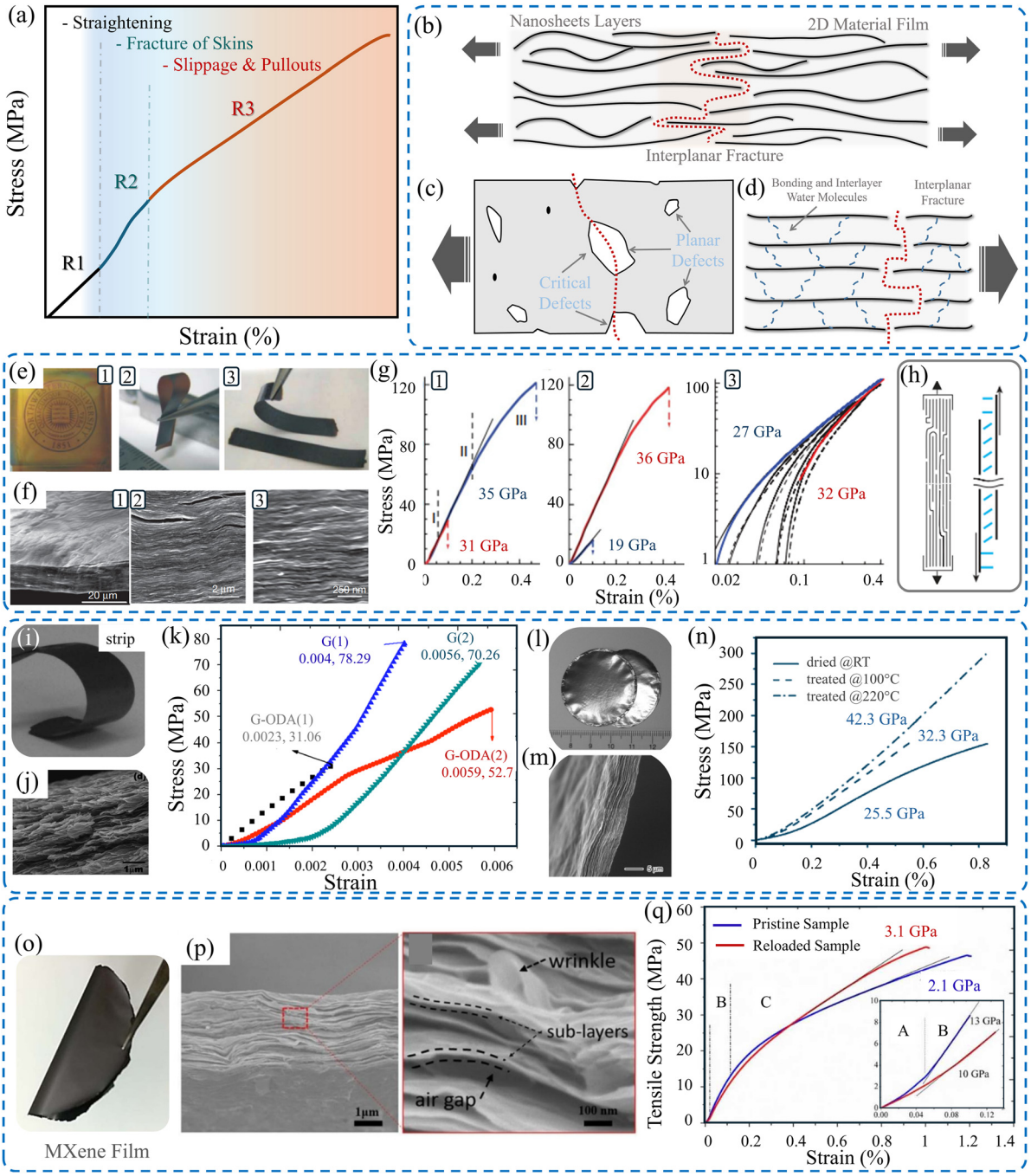

Fig. 2 (a) Typical stress–strain curve of 2D material films.[44] Schematic of (b) interplanar fracture of a film made of 2D material, (c) bonding between adjacent layers, and (d) side critical defects and planar defects. Reproduced with permission.[90] Copyright © 2015, the American Chemical Society. (e) Image of prepared GO films with thicknesses of (1) ~1 μm, (2) ~5 μm, and (3) ~25 μm. (f) SEM images of the cross-section of a 10 μm thick GO film. (g) Stress–strain curves of GO films with various thicknesses. (h) Schematic of uniaxial tensile loading showing the water molecules connecting the individual GO nanosheets. Reproduced with permission.[109] Copyright © 2007, Springer Nature Limited. (i) Images of a freestanding rGO strip. (j) SEM image of the fracture surface. (k) Stress–strain curves of the tested samples. Reproduced with permission.[32] Copyrights © 2011, AIP Publishing. (l) and (m) Images of the rGO film's surface and the film's cross-section. (n) Stress–strain curves of rGO films. Reproduced with permission.[107] Copyright © 2008 WILEY-VCH Verlag GmbH & Co. KGaA, Weinheim. (o) Image of freestanding $Ti_3C_2T_x$ MXene film. (p) SEM image of the fracture surface of $Ti_3C_2T_x$ film due to tensile loading. (q) Stress–strain curves of the MXene films (inset: magnified image of stages A and B). Reproduced with permission.[106] Copyrights © 2020, IOPSCIENCE.

stage, the ripples and waviness of the sample are straightened under the effect of the applied force. The second stage (R_2) includes the failure of the film's skin. This stage shows a higher Young's modulus. Finally, the third stage (R_3) enters the slippage and pulls out of the nanosheets. Such analogous behavior was observed for GO[44] and $Ti_3C_2T_x$ MXene films,[106] which are

discussed in more detail in the subsequent subsections. Overall, the typical stress–strain curve of films is similar to that obtained for polymeric materials.[20,107–109] This behavior originated basically from existing irregularities, such as surface waviness, flake wrinkles, and internal voids. Fig. 2b–d schematically illustrates the defects and voids that initiate the propagated cracks due to loading.

3.1. Graphene

Graphene and its derivatives have been pioneer members of the 2D materials family since its first successful exfoliation.[49] Unveiling their exceptional properties opened a revolutionary era of 2D materials, which later gained abundant potential in many applications.[110] GO is a derivative of graphene, retaining the extraordinary mechanical properties of graphene. It is a layered substance composed of hydrophilic oxygenated graphene nanosheets featuring oxygen determination groups on its end edges and basal planes.[111]

The mechanical properties of pristine GO films have been elucidated under uniaxial tensile loading by Dikin *et al.*[109] Fig. 2e shows the produced freestanding GO films with different thicknesses *via* VAF. The morphology of the fracture surface, captured *via* SEM (Fig. 2f), shows a well-packed layered structure in which the nanosheets are intricately interconnected in a nearly parallel manner throughout the cross-section. Moreover, 100–200 nm thick wavy top and bottom skins with lower density are observed. The results demonstrate three regimes of deformation of the stress–strain curve, as presented in Fig. 2g. The initial stage is associated with the straightening of wrinkling and the waviness of the nanoflakes. This stage is quite small. Although the pull-out phenomenon is expected when loaded beyond the elastic stage, no pull-out is observed on the fracture surface. For a better understanding of the elastic regime, reloading and unloading cycles of the samples were conducted, which showed permanent deformation of the samples. The modulus of elasticity was found to rise by about 20% after five loading–unloading cycles, which indicated a self-reinforcing phenomenon due to the stretching and alignment of the flakes. This produces more intimate contact between the individual sheets, leading to a stiffer structure analogous to the aligning of polymer chains under tensile loading. Additionally, the wrinkled and corrugated morphology of the assembled nanoflakes contributed to uniform load distribution, which led to greater resiliency of the entire macroscopic film. The explanation for the mechanics of failure clarified that the load is transferred between the flakes through shear deformation, which primarily concentrates on the interlamellar interaction that involves hydrogen-bonded water molecules, as shown in Fig. 2h. Thus, a straight, brittle-like fracture path without extensive pull-out features was observed.

The mechanical properties of neat reduced graphene oxide (rGO) film were investigated by Ranjbartoreh *et al.*[32] Freestanding rGO films were fabricated *via* the VAF process, as shown in Fig. 2i. Uniaxial tensile tests were conducted on rectangular strips (Fig. 2j). The strips are 30 mm × 5 mm with 3 μm thickness. rGO films exhibited a tensile strength of 78.29 MPa, Young's modulus of 31.69 GPa, and failure strain of around 0.4%, as presented in Fig. 2k. Observation of the fracture surface reveals the interlock tiles-like structure of the nanosheets. The results show strain rate dependency, which is discussed later in a separate section. Similarly, Chen *et al.*[107] experimentally investigated the mechanical properties of rGO film fabricated *via* VAF, as shown in Fig. 2l. SEM images of the film's surface and cross-section (Fig. 2m) show a smooth surface and orderly packed rGO nanosheets. The tensile strength, Young's modulus, and elongation at failure of 6 μm thick films were found to be about 150 MPa, 20.5 GPa, and 0.8%, respectively, as presented in Fig. 2n. The thermal reduction of GO to rGO in a macroscopic film was successfully achieved by David and Singh.[112] The thermally reduced GO showed mechanical properties comparable to those made by chemical reduction. These are discussed in detail in the section on the influence of annealing treatment.

3.2. MXenes

MXenes are an emerging family of 2D materials comprising transition metal carbides or nitrides. Its general chemical formula is $M_{n+1}X_nT_x$ (n = 1–4), where M is an early transition metal layer interleaved by the X element representing either nitride or carbide, and T is a surface termination group, most likely hydroxyl (–OH) or fluoride (–F).[113] These chemically stable, 2D layered nanomaterials were proposed to be called "MXene" to highlight its unique graphene-like morphology.[114] The MXene family of materials has rapidly expanded since reporting the synthesis of titanium carbide ($Ti_3C_2T_x$) in 2011.[115] MXenes exist in the form of various atomic structures, varying from, for instance, M_2XT_x to $M_3X_2T_x$, $M_4X_3T_x$, and $M_4X_3T_x$.[114] This variation offers adjustability and the potential to explore tailorable properties. Additionally, the MXene family has broadened to encompass more intricate atomic structures, such as ordered double-transition metal MXenes, which have the formulae of $M'_2M''C_2$ and $M'_2M''_2C_3$.[113] The various reported MXenes were demonstrated in.[116,117] Accordingly, they possess stability with remarkable properties over time.[118] With the massive interest in MXenes, improving the utilized MAX phases,[119] developing new synthesis methods for preparing MAX phases,[120] and enhancing the known procedure for the etching process,[121] several MXenes have been prepared to date.[116]

Among the 2D materials, MXenes ($Ti_3C_2T_x$) exhibit the highest stiffness due to their natural structure, comprising more than three atomic layers. The tensile behavior, deformation, and fracture mechanism of 2–17 μm thick MXene ($Ti_3C_2T_x$) films (Fig. 2o) were investigated under both quasi-static tension and cyclic tension loading.[106] Fig. 2q illustrates stress–strain curves of the tested $Ti_3C_2T_x$ MXene samples. The failure and fracture mechanisms were found to be highly sensitive to relative sliding between layers, as demonstrated for the GO and rGO films. The measured elastic modulus was recorded to be 15 ± 4 GPa, compared to 330 GPa for the monolayer of $Ti_3C_2T_x$.[16] It is practical to consider the stretching of $Ti_3C_2T_x$ flakes, which contributes to the overall tensile deformation. The fracture of $Ti_3C_2T_x$ films was brittle, similar to those films made of GO and rGO. This brittle failure indicates rapid crack propagation throughout the sample's width, as shown in

Fig. 2p, where an SEM image of the fracture surface of the film made of $Ti_3C_2T_x$ is shown. It is obvious that the fracture surface is flat and straight without obvious signs of necking or delamination. Pulling out of the sublayers is observed. In addition to straining the nanosheets during tensile loading, the tensile load is also transferred between overlapping sheets by shear stress, which causes slipping and pulling out of the nanoflakes. Finally, voids between adjacent flakes form a critical crack that propagates rapidly until failure.

Assessing the mechanical properties of 2D material films requires systematic investigation because their performance highly depends on several parameters. The mechanical properties of various 2D material films in terms of material type, fabrication technique, and film's thickness are summarized in Table 2. It is obvious that the mechanical properties of such films have a large range of variations, indicating the importance of the preparation stages of these films.

4. Factors affecting the mechanical properties of 2D material films

Although the assessment of the tensile properties of neat 2D material films seemed to be a straightforward process,

Table 2 Mechanical properties of various 2D material films

2D material	Fabrication technique	Film thickness (μm)	Young's modulus (GPa)	Tensile strength (MPa)	Toughness MJ m^{-3}	Strain (%)	Ref.
rGO	VAF	3	31.69	78.29	—	0.4	32
rGO	VAF	6	20.5	∼150	—	∼0.82	107
rGO	VAF	3–5	27	132	—	0.54	122
rGO	VAF	10	∼0.47	∼16	—	∼3.5	112
rGO	VAF	—	—	165.8 ± 1.1	2.4 ± 0.4	3.7 ± 0.3	123
rGO	VAF	3	1.6 ± 0.1	307.8 ± 6.4	—	7.5 ± 0.4	124
rGO	CCC	—	—	∼660	—	∼3.2	125
rGO	Electro-spray deposition	—	6.84	66	—	1.2	126
GO	VAF	5.2–11	32	60–85	—	0.6	109
GO	VAF	4.9	—	56.7 ± 2.3	0.62 ± 0.015	2.5 ± 0.3	44
GO	VAF	9.4	—	60.9 ± 2.6	1.42 ± 0.36	3.9 ± 0.4	44
GO	VAF	5.4	4.2 ± 0.1	169.3 ± 2.1	—	9.2 ± 0.2	124
GO	Casting	4.9	—	59.6 ± 16	0.78 ± 0.17	3.2 ± 0.6	44
GO	Casting	7.6	—	78.5 ± 7.7	1.66 ± 0.19	3.9 ± 0.3	44
GO	Casting	10.5	—	62.6 ± 5.3	2.12 ± 0.41	4.2 ± 0.5	44
GO	Casting	12.5	—	84.5 ± 9.8	4.37 ± 0.94	9.8 ± 1.9	44
GO	Casting	13.8	—	71.2 ± 11	3.46 ± 0.73	8.2 ± 0.7	44
GO	Casting	15.7	—	70.8 ± 5.1	3.23 ± 0.53	7.0 ± 0.5	44
GO	VAF	—	—	82.2 ± 1.8	0.9 ± 0.05	2.6 ± 0.3	123
GO	VAF	35	∼19	—	—	—	127
GO	Blade coating	6	—	∼87	—	∼1.5–3.5	128
GO	Blade coating	10	—	∼210	—	∼0.9	129
GO	Blade coating	30	—	122	—	2.2	130
GO	Blade coating	40	9–10	50.5	0.242	0.81	131
GO	CCC	—	—	∼157	—	∼3.4	125
GO	VAF	6	—	187 ± 18	—	∼2.5	132
GO	Spray coating	6	—	774 ± 46	—	∼3	132
GO	Casting	10	4.1 ± 0.66	67.1 ± 12.3	—	2.44 ± 0.27	20
GO	VAF	12	16.6	149.4	—	1.65	133
GO	VAF	12	10.8	119	—	2.13	133
GO	VAF	—	25.6 ± 1.1	81.9 ± 5.3	—	0.4 ± 0.03	134
GO	VAF	7	9.1 ± 0.6	64.6 ± 3.3	—	∼1.0	135
GO	VAF	—	10.5	63.6	—	∼1.0	136
$Ti_3C_2T_x$	VAF	2.3-17	14 ± 4	50 ± 15	—	0.89 ± 0.40	106
$Ti_3C_2T_x$	VAF	∼10	2.53 ± 0.11	28.92 ± 4.24	0.67 ± 0.20	3.46 ± 0.65	137
$Ti_3C_2T_x$	VAF	∼10	—	25.22 ± 2.34	0.22 ± 0.04	1.28 ± 0.13	138
$Ti_3C_2T_x$	VAF	—	3.1 ± 0.05	18.2 ± 1.8	0.11	1.3 ± 0.3	139
$Ti_3C_2T_x$	VAF	—	∼5	∼44.3	∼0.365	∼1.4	140
$Ti_3C_2T_x$	VAF	40	1.6 ± 0.2	14.2 ± 2.1	0.06	∼1	141
$Ti_3C_2T_x$	VAF	—	—	61.2 ± 2.3	0.7 ± 0.01	2.3 ± 0.5	123
$Ti_3C_2T_x$	VAF	6	—	87 ± 13	—	∼0.5	132
$Ti_3C_2T_x$	VAF	2.7	9.4 ± 0.3	90.4 ± 1.2	—	1.5	124
$Ti_3C_2T_x$	Blade coating	1.7	21.5 ± 0.8	146.4 ± 2.9	0.6 ± 0.1	0.8 ± 0.1	142
$Ti_3C_2T_x$	Blade coating	∼0.94	20.6 ± 3.1	568 ± 24	3.0 ± 0.3	3.2 ± 0.2	143
$Ti_3C_2T_x$	Blade coating	∼2.4	18.3 ± 2.8	480 ± 35	8.4 ± 0.6	3.0 ± 0.3	143
$Ti_3C_2T_x$	VAF	1.2	2.2 ± 0.4	41 ± 5.1	0.6 ± 0.1	2.5 ± 0.4	143
$Ti_3C_2T_x$	Blade coating	2.7	9.5 ± 0.7	185 ± 6	2.36 ± 0.02	2.99 ± 0.04	144
$Ti_3C_2T_x$	Spray coating	5	66	707 ± 62	—	∼1	132
$Ti_3C_2T_x$	VAF	∼10	∼5	19	—	∼0.6	145
$Ti_3C_2T_x$	VAF	10	—	36	—	∼1.5	146
$Ti_3C_2T_x$	VAF	7	—	23 ± 8	0.1 ± 0.03	∼1.65	147
$Ti_3C_2T_x$	VAF	—	96.4 MPa	19.03	0.06	0.38	148

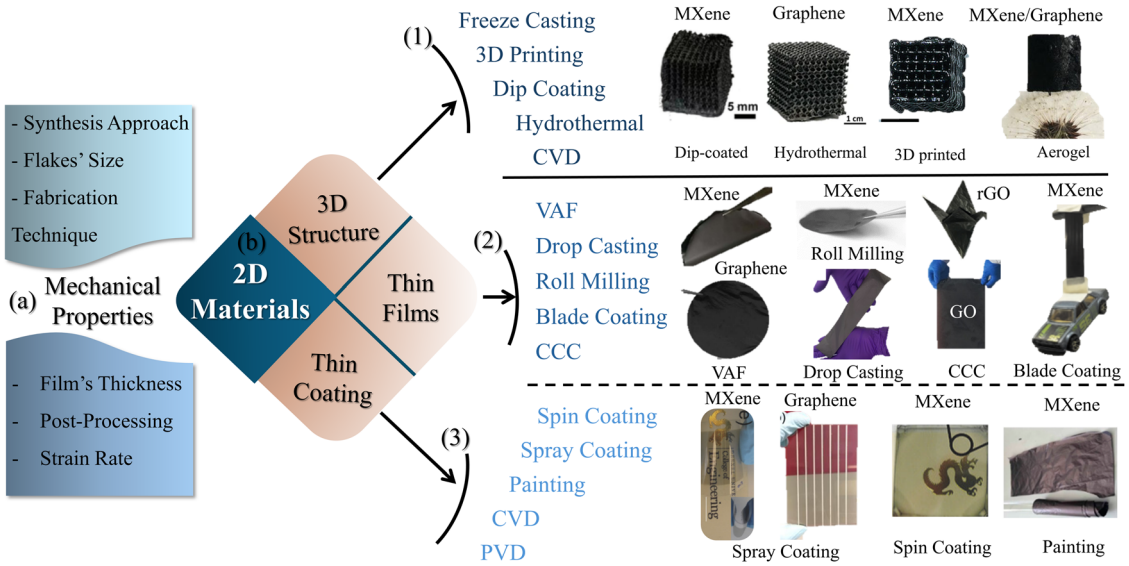

Fig. 3 (a) Factors affecting the mechanical properties of 2D material films. (b) Fabrication techniques of various 2D material structures: (1) 3D structures,[150–153] (2) thin films,[32,42,106,125,143,154] and (3) thin coatings.[155–158]

dedicated setups may be required, particularly for very thin films. Smooth grippers with well-defined gripping pressure and length are essential for proper testing.[149] Moreover, Wan *et al.*[144] showed that adhesion of the specimen on a rigid paper frame, with a suitable hole, facilitated the mounting of the specimen and eliminated the initial damage due to loading. Additionally, many factors, such as synthesis method, nanoflakes size, fabrication techniques of the film, post-processing, specimen's thickness, and the applied strain rate, affect the resulting mechanical properties, as illustrated in Fig. 3a. The influence of these factors originates from their impact on the nanoflake alignment and the interlayer characteristics, which profoundly affect the overall mechanical properties of the films.

4.1. Effect of the synthesis method

The utilized synthesis method utilized for 2D materials affects the properties of individual nanoflakes, which in turn impacts the mechanical properties of the acquired films. For instance, MXene films made of nanoflakes prepared by the minimally intensive layer delamination (MILD) approach (*in situ* HF formation) showed better mechanical properties than flakes prepared by applying the direct HF-acid etching technique.[159] This was explained by the fact that the former etching technique produced flakes with larger lateral sizes and low defect levels.[160]

4.2. Effect of fabrication techniques on films

The versatile process of synthesizing 2D materials in a manageable way is one of their distinct merits. They can be processed into freestanding samples in various forms, from thin coatings and films to bulk 3D structures. Extremely thin coatings of 2D materials can be achieved either by CVD,[161,162] PVD,[163] spray coating,[157] spin coating, or painting technique.[158] Thicker freestanding thin films can be fabricated *via* VAF,[164] drop casting (DC),[42] roll milling,[154] spray coating,[156] spin coating,[155] and blade coating techniques.[165] Furthermore, 3D structures, composed of 2D materials, can be obtained *via* freeze drying,[166] freeze casting,[167] dip coating,[150,151] 3D printing,[152] hydrothermal coating,[150] and CVD. It is worth mentioning that dip coating on well-designed scaffolds, by 3D printing, offers intricate 3D architectures made from 2D materials.[168,169] On the contrary, stochastic aerogel structures processed by freeze drying and spongy structures of 2D material obtained utilizing dip coating show less controllability. Recently, conformal coating *via* the self-assembly of MXene nanoflakes on metal powder has been achieved, opening doors for advancing additive manufacturing technologies.[170]

Converting 2D materials from aqueous solution or powder form into thin film provides the ability to tune the properties of the films. The alignment of the 2D flakes and the interlayer characteristics of the film may be controlled using fabrication techniques. Consequently, preferable mechanical properties can be achieved. Ye *et al.*[44] analyzed systemically the influence of fabrication technique on both tensile and fracture properties of macroscopic GO films. VAF and casting processes (Fig. 4a and b) were employed to fabricate freestanding F-GO and C-GO films, respectively. The mechanical properties of the films can be modulated by the assembled structure. The skin-wrinkles-skin structure resulting from the fabrication process plays a significant role in defining the elongation to fail, as shown in Fig. 4f. An examination of the fracture surface showed a uniform cross-section with a well-packed and highly ordered layered (straight and smooth sides) structure for the F-GO films. However, C-GO films exhibit a lamellar and loose microstructure with obvious interlayer gaps (waved and corrugated edges). This apparently loose microstructure is explained by the absence of normal stresses, which in turn leads to misalignments of GO flakes during the casting process, unlike VAF, which provides a more compact structure due to pressure, as

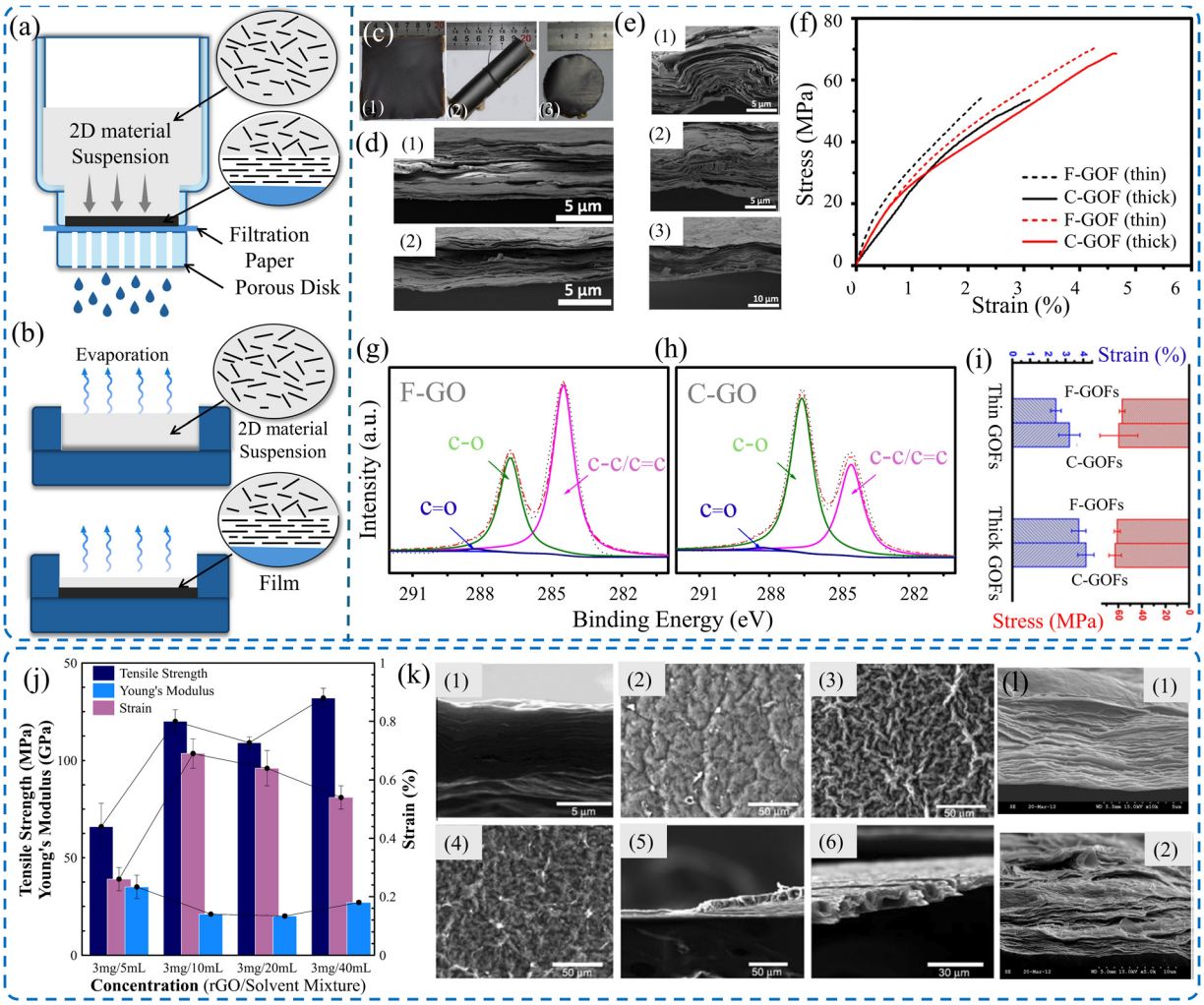

Fig. 4 Schematic of (a) VAF and (b) drop casting techniques. (c) Images of (1 and 2) casted film and (3) filtered film. SEM images of (d) cross-sectional images showing the upper and lower skins. (e) Crumples and interlocks of thick C-GOFs. (f) Stress–strain curve of casted and filtered GO films. XPS spectra of (g) VAF GO and (h) cast-GO films. (i) Comparison between thin and thick films.[44] (j) Effect of solvent concentration on the mechanical properties of rGO films prepared by VAF process. (k) SEM images of rGO film cross sections and surfaces prepared using different concentrations. (l) SEM images of the cross-sections of the fracture surface. Reproduced with permission.[122] Copyright © 2012, Elsevier Ltd.

shown in Fig. 4d. F-GO films have a lower failure strain, attributed to the lack of hydrogen bonds, and the compact structure has lower interlayer gaps compared to those made from casting. The relatively high interlayer gaps in the C-CO films provide more space for the alignment and slippage of flakes under loading; thus, their elongation at failure is larger. X-ray photoelectron spectroscopy (XPS) spectra, shown in Fig. 4g-h, illustrate the deconvolution of the C 1s core level spectrum for F-GO and C-GO, respectively. There is a drop in the total peak area of oxygen functionalities from 61.6% to 36.5% for C-GO and F-GO films, respectively, which indicates that the casting technique attained more oxygen functional groups. These oxygen functional groups can form hydrogen bonds and play a direct role in defining the mechanical properties of the films obtained.[171,172]

Although VAF is deemed a straightforward process and is widely employed for fabricating freestanding 2D material films, VAF is a sensitive process that may impact the properties of the acquired films. For instance, the concentration of colloidal suspensions may influence the mechanical properties of the films obtained. Park *et al.*[122] investigated the concentration effect of rGO films, as shown in Fig. 4j. It was demonstrated that the rGO films fabricated using low concentrations (3 mg/40 mL) had enhanced elastic modulus and tensile strength, resulting in smooth surface morphology compared to films acquired using higher concentrations (3 mg/20 mL and 3 mg/10 mL) (Fig. 4k and l). However, low concentrations led to films with a lower failure strain (0.54%) compared to those obtained using higher concentrations.

For VAF, a lower volume of GO colloids leads to an effective fabrication process with a highly compacted structure because of the assembly forces on the entire volume. However, for higher volumes of GO colloids, the vacuum process becomes more susceptible to hindrances. Blocking the collecting

membrane due to the initial deposition of GO sheets makes it challenging to assemble the remaining GO colloids. Consequently, this phenomenon contributes to a slowdown in the filtration process, which resembles an evaporation process. Occasionally, a skin-wrinkles-skin structure can be observed in thick F-GO films, leading to enhanced tensile strength and elongation at failure, as shown in Fig. 4i. Additionally, the nature of the casting process induces wrinkled constructions with relatively high misalignment, crumples, and interlocks, as shown in Fig. 4e. Obviously, the thicker C-GO films have a higher proportion of wrinkled and interlocked regions, leading to higher tensile strength and elongation at failure. One can also notice that, even for thick films, the mechanical properties of GO films fabricated by casting still outperform those of the VAF process.[44]

VAF and casting processes are extensively used in a wide range for the fabrication of 2D material films; interestingly, the optimized blade coating technique (Fig. 5a) provides a scalable approach for the production of films with extremely high mechanical properties. Additionally, the applied shear rate, the suspension's concentration, and viscosity can be optimized to acquire isotropic mechanical properties.[143] Chen *et al.*[128] produced large-scale GO films by applying the blade coating technique, as depicted in Fig. 5d. It was demonstrated that the produced GO films produced had a tensile strength of about 87 MPa. Peng *et al.*[129] reported strong GO films with a tensile strength of about 210 MPa. Freestanding MXene films (Fig. 5b) of about 1 μm thickness, fabricated *via* blade coating, can achieve a tensile strength of 570 MPa and Young's modulus of 20.6 GPa.[143] They outperform those fabricated *via* VAF, which have a tensile strength of about 40 MPa (Fig. 5c). Similarly, Wan *et al.*[144] showed that MXene films made using blade coating techniques exhibited extraordinary mechanical properties, where tensile strength of 185 MPa and Young's modulus of 9.5 GPa were reported.

As a modified casting process, the continuous centrifugal casting (CCC) technique (Fig. 5e) was introduced as a scalable and efficient approach to fabricate robust 2D materials films by Zhong *et al.*[125] This technique combines the advantages of aligned flakes, densified structure, and short production time, and it can be used to fabricate mechanically superior GO and rGO films, as shown in Fig. 5f. The films produced have comparable mechanical properties with those made *via* blade coating,[143] as shown in Fig. 5g. Furthermore, spray coating *via* spatially confined evaporation (Fig. 5h) can produce very thin MXene films with enhanced aligned flakes.[132] The modified technique yields a wrinkled-free surface compared to those made using conventional techniques, which have crumpled structures (Fig. 5i). The root-mean-square (RMS) roughness measurements (Fig. 5k) show that the films have smoother surfaces than those made *via* VAF. Moreover, the thinner the film, the smoother the film's surface. The fabricated films have an ultra-high tensile strength of 707 MPa and Young's modulus of 66 GPa compared to only 87 ± 13 MPa for those made by VAF. Similarly, the tensile strengths of GO films produced by spray coating and VAF are 774 ± 46 and 187 ± 18 MPa, respectively, as demonstrated in Fig. 5l.

4.3. Effect of the size of nanoflake (packing density)

Films of 2D materials are assembled structures comprising stacked 2D nanoflakes. The obtained properties of such thin structures highly depend on the lateral size of the flakes. Accordingly, the superior mechanical properties of 2D material films can be attained by controlling the size of the nanoflakes. The size of tuning flakes defines the level of defects, such as voids, which affect the degree of connection between adjacent flakes. Generally, a large flake size is preferred for constructing high-performance films because they contain highly oriented flakes. Utilizing large flakes induces films with a low packing density due to the large voids that might exist. In contrast, films fabricated from small nanoflakes entail smaller voids, high packing density, and a higher number of interlayer connections but less oriented structures. Thus, adjusting the densification level, flake orientation, and interfacial connection by opting for an appropriate flake size can control not only the overall mechanical properties of the film but also the thermal and electrical properties.[173]

The mechanical properties of GO films fabricated *via* blade coating, in association with flake lateral size, were studied by Lin *et al.*[173] It was proven that GO films made of large flakes (40–50 μm) have higher tensile strength and strain to failure compared to those constructed of small flakes (5–8 μm). The former achieved a tensile strength and failure strain of 52.6 MPa and 1.93%, respectively, representing an enhancement of about 150% and 168%, respectively, over those with a smaller flake size, as shown in Fig. 6a. The enhanced behavior was explained by the fact that the larger flakes had fewer defects and more effective π–π interaction between adjacent GO flakes. This is confirmed by XPS analysis (Fig. 6b), which shows that large flake GO films possess a higher carbon to oxygen (C/O) ratio of 2.12 compared to 1.85 for small flake films. Additionally, Raman spectra show that large flake films demonstrated lower I_D/I_G, indicating fewer oxygenated groups and fewer defects, as shown in Fig. 6c. A similar size effect was observed for rGO films fabricated using the CCC technique. It was demonstrated that large-flake-films (20 μm) have a higher tensile strength of about 660 MPa compared with small-flake-films (1 μm) which have a tensile strength of about 320 MPa.[125]

Advances in the synthesis of the 2D materials with controlled lateral sizes allow for modulation of their performance. Large-sized MXene flakes can be synthesized either by applying the MILD process or the direct HF etching approach. MXene flakes with lateral size (10–13 μm) can be obtained *via* an optimized MILD process, either by tuning the size of parent MAX phase[143] or selectively opting for large-size flakes *via* centrifugation.[144] However, a direct HF approach with a soft delamination approach can be applied for the synthesis of ultra-large flakes (larger than 40 μm).[37] Additionally, it was demonstrated that MXene flakes with specific sizes can be opted for by optimized centrifugation.[174] Combining the advantage of producing large flakes with the ability to separate

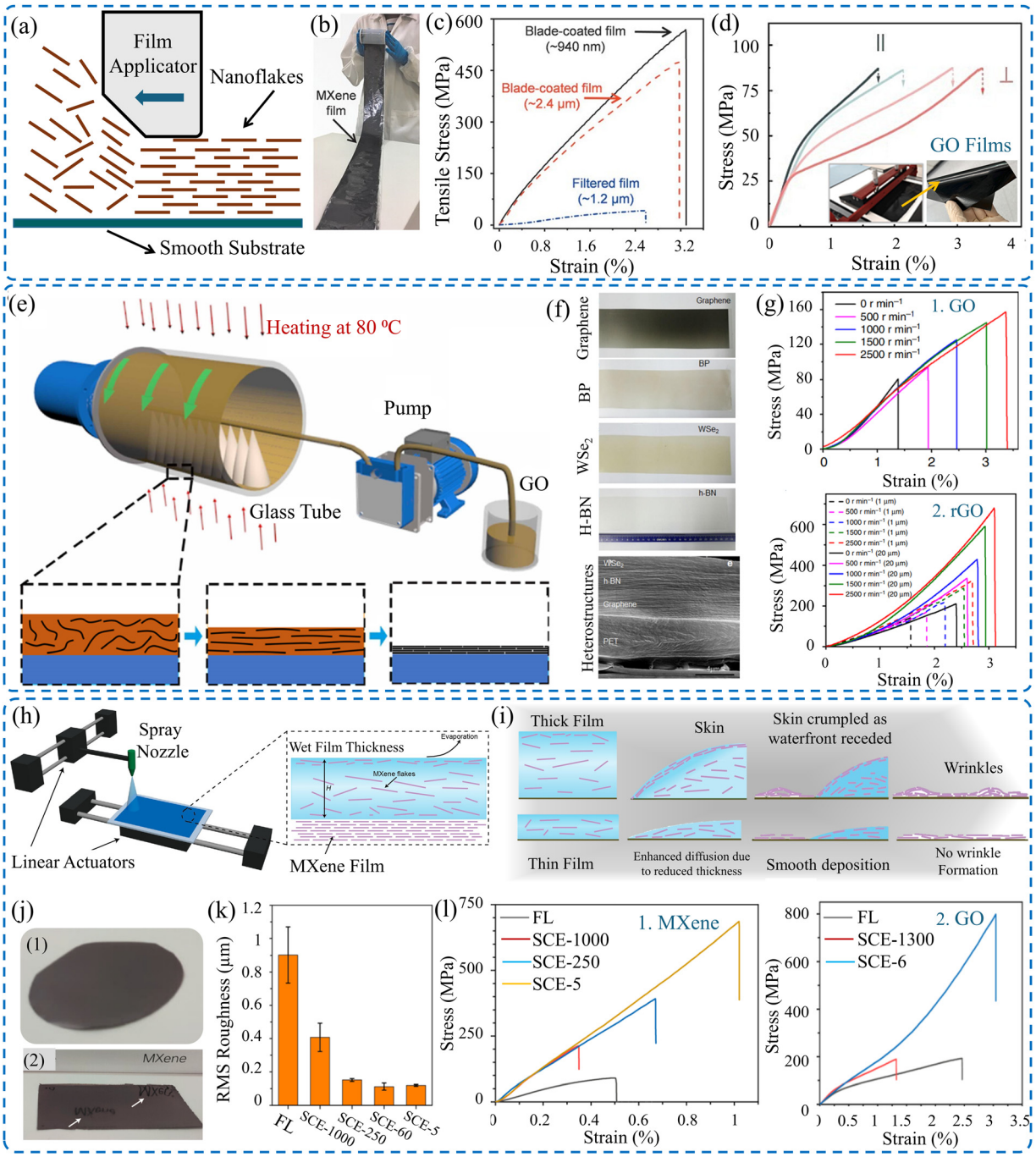

Fig. 5 (a) Schematic of the blade coating technique. (b) Digital images of MXene film made by blade coating. (c) Effect of the fabrication technique on the tensile strength of the MXene films. Reproduced with permission.[143] Copyrights © 2020, WILEY-VCH Verlag GmbH & Co. KGaA, Weinheim. (d) Tensile strength of GO films made *via* blade coating and images of the film applicator and GO film.[128] (e) Schematic of continuous centrifugal casting technique. (f) Image of various 2D material films fabricated *via* continuous centrifugal casting. (g) Stress–strain curves of GO and rGO films.[125] Schematic of (h) spray coating with spatially confined evaporation, and (i) difference between thin and thick films. (j) Difference between films obtained *via* (1) VAF and (2) modified spray coating. (k) Root-mean-square (RMS) roughness measurements as a function of the film's thickness. (l) Stress–strain curves of the obtained (1) MXene and (2) rGO films. Reproduced with permission.[132] Copyright © 2023, the American Chemical Society.

specific sizes opens doors to obtain high-performance film structures.

The impact of nanosheet size on the resultant mechanical properties of $Ti_3C_2T_x$ MXene film has been experimentally investigated.[106] Ultrasonication of as-synthesized $Ti_3C_2T_x$ MXene flakes was adopted to control the size of the flakes. Ultrasonication of MXene flakes for a controlled time interval can break down the flakes into a few hundred nanometers in their lateral dimensions. Fig. 6f shows the lateral size of the MXene flakes after various ultrasonication times. It is obvious that films made

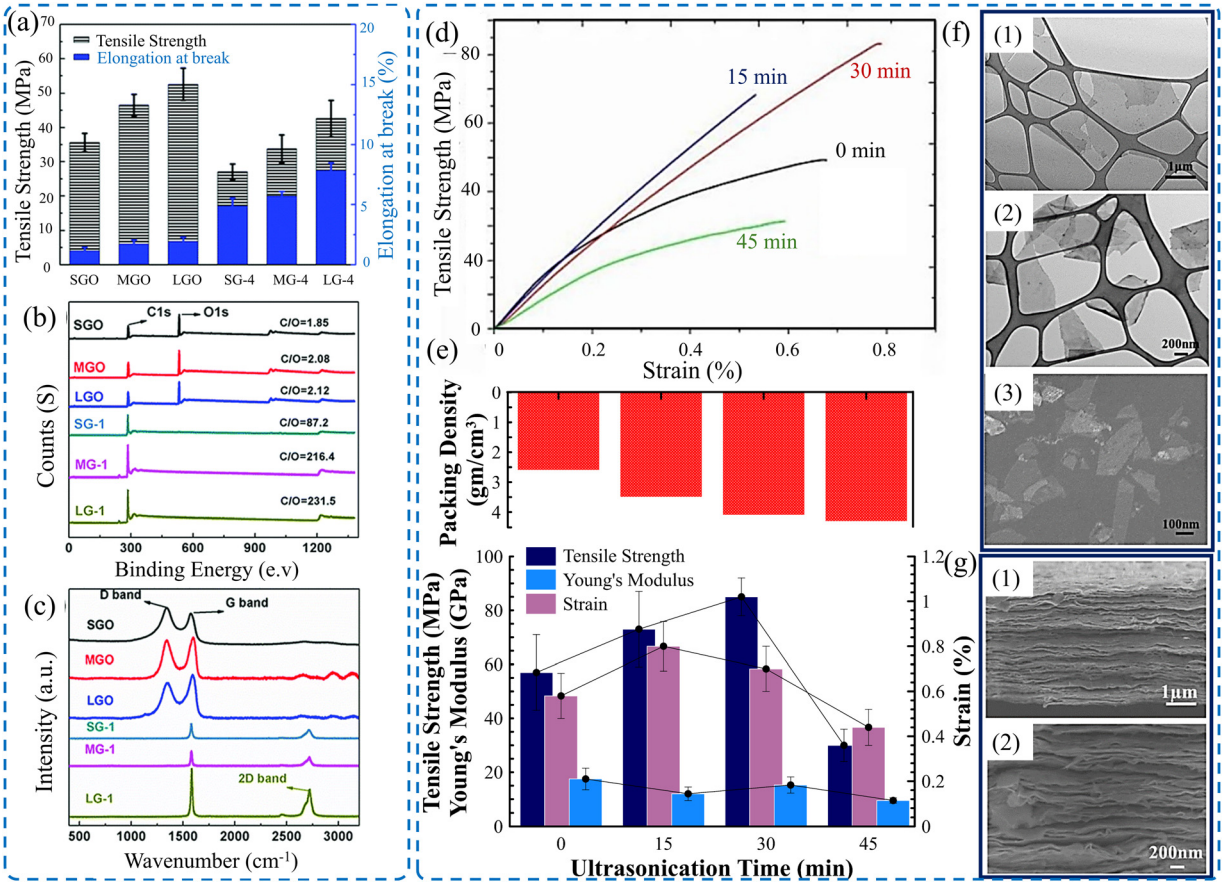

Fig. 6 (a) Bar chart showing the influence of GO flake size on the mechanical properties of the GO film. (b) XPS spectra and (c) Raman spectra of GO films constructed from different flake sizes.[173] (d) Stress–strain curves of MXene films with different flake sizes (ultrasonication for different time intervals). (e) Obtained packing density and the corresponding tensile strength, Young's modulus, and failure strain for various ultrasonication times. (f) TEM image of nanoflakes after (1) 15, (2) 30, and (3) 30 min of ultrasonication. (g) SEM images of a cross-section of MXene films constructed from (1) small and (2) large flake sizes. Reproduced with permission.[106] Copyrights © 2020, IOPSCIENCE.

of small flakes have a higher packing density and a well-packed structure (Fig. 6g) compared to those made of large flakes. The resulting mechanical properties show dependency on the flake size. The tensile strength increases with the reduction of flake size, reaching about 85 MPa for films made of flakes sonicated for 30 min, as shown in Fig. 6d and e.

The effect of flake lateral size on the mechanical properties of MXene films made *via* VAF and blade coating was investigated by Zhang *et al.*[143] For both fabrication techniques, MXene films composed of large flakes (~10 μm) have better mechanical properties than those made of smaller flakes (~200 nm). For VAF, the large-flakes-films have about twice the tensile strength and toughness and three times the strain to failure compared to those of small-flakes-films. However, more augmentations were observed for films made *via* blade coating. Large-flake MXene films attained higher tensile strength, toughness, and strain to failure by about 360%, 2500%, and 350%, respectively, as illustrated in Table 3.

Similarly, Wan *et al.*[144] reported the effect of the flake's size on the porosity level and, consequently, the mechanical properties of MXene films made *via* blade coating. It has been demonstrated that large-flake films outperform small-flake films. Although the large-flake MXene films have a higher level of porosity (16.1%), they have tensile strength and toughness of about 185 MPa and 2.36 MJ m^{-3} with 43% and 390% enhancement, respectively, compared to small-flake MXene

Table 3 Effect of flake size on the mechanical properties of MXene films[143]

2D material	Flake lateral size (μm)	Film thickness (μm)	Fabrication technique	Tensile strength	Young's modulus (GPa)	Toughness (MJ m^{-3})	Strain to failure (%)
$Ti_3C_2T_x$	~10	~1.2	VAF	41 ± 5.1	2.2 ± 0.4	0.6 ± 0.1	2.5 ± 0.4
$Ti_3C_2T_x$	~200 nm	~1.4	VAF	20 ± 3.5	3.5 ± 0.3	0.3 ± 0.07	1.0 ± 0.3
$Ti_3C_2T_x$	~10	~0.94	Blade coating	568 ± 24	20.6 ± 3.1	10.2 ± 0.3	3.2 ± 0.2
$Ti_3C_2T_x$	200 nm	~1.1	Blade coating	123 ± 6.7	13.3 ± 0.2	0.4 ± 0.05	0.7 ± 0.2

Table 4 Effect of flake size on the mechanical properties of MXene films made *via* blade coating[144]

2D material	Flake lateral size (μm)	*d* (nm)	Film thickness (μm)	Porosity (%)	Tensile strength (MPa)	Young's modulus (GPa)	Toughness (MJ m^{-3})	Strain to failure (%)
$Ti_3C_2T_x$	0.35	1.43	2.8 ± 0.1	3.84 ± 0.38	127 ± 13	22.8 ± 1.7	0.48 ± 0.10	0.68 ± 0.06
$Ti_3C_2T_x$	13.5	1.25	2.7 ± 0.1	16.1 ± 0.6	185 ± 6	9.5 ± 0.7	2.36 ± 0.02	2.99 ± 0.04
Mixture of small and large	10% small + 90% large	1.29	2.8 ± 0.2	9.06 ± 0.32	409 ± 26	13.7 ± 1.0	4.12 ± 0.56	2.79 ± 0.15

films (3.84% porosity). However, small-flake MXene films have a higher Young's modulus and strain to failure by about 140% and 340%, respectively, compared to large-flake films, as summarized in Table 4. Certainly, films made from a mixture of small and large flakes show better mechanical performance. This behavior is discussed later in the Densification section.

4.4. Effect of film's thickness

Thickness is another parameter that influences the mechanical properties of the 2D material films. It is demonstrated that the film's thickness slightly affected the acquired mechanical properties for both F-GO and C-GO films when the thickness was increased from 4.9 μm to 9–10 μm.[44] For thick F-GO films, the resulting tensile strength and elongation were improved to 60.9 ± 2.6 MPa and 3.9 ± 0.4%, respectively. Similarly, these results were improved to 62.6 ± 5.3 MPa and 4.2 ± 0.5%, respectively, for thick C-GO films. The reason behind this is the assembly mechanism of the nanoflakes during the fabrication process. It was demonstrated that for a film thickness of 4.9 μm, there was a minor difference in the average tensile strengths between F-GO (56.7 ± 2.3 MPa) and C-GO films (59.6 ± 16 MPa). However, there is a noticeable enhancement of elongation by ~31% of C-GO films compared to F-GO films, as shown in Fig. 7a. Similarly, the mechanical properties of GO films in terms of film thickness were investigated by Liu *et al.*[127] It is obvious that both the tensile strength and the elastic modulus deteriorate with a high thickness. However, the strain to failure increases for thicker films, as shown in Fig. 7d. The same trend is noted for GO films made by coating with a spatially confined evaporation technique, as shown in Fig. 7e.

Additionally, the mechanical properties of MXene films made *via* VAF,[106] and blade coating[143] are sensitive to film thickness, as shown in Fig. 7b and c. Similarly, MXene films acquired *via* Spray coating with Spatially Confined Evaporation were also sensitive to film thickness.[132] Thin MXene films (5 μm) have higher, enhanced tensile strength and Young's modulus by over 200% and 10%, respectively, compared to thicker films.

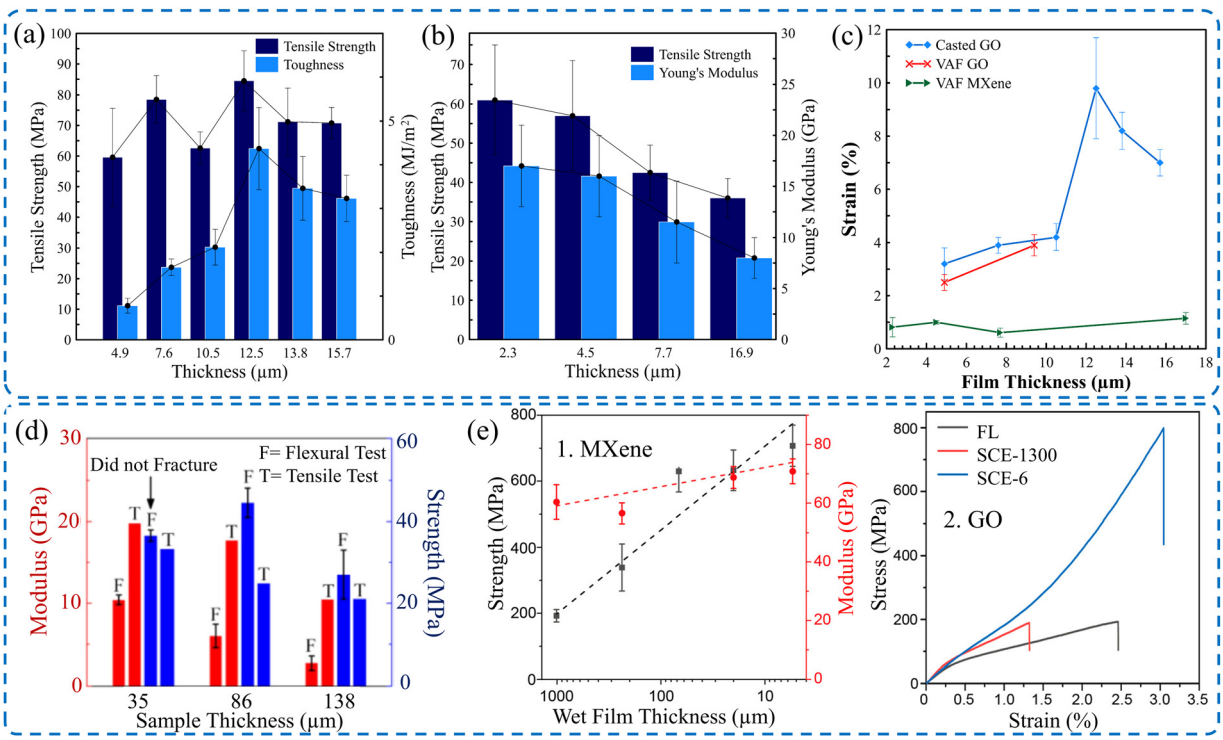

Fig. 7 Effect of film's thickness on (a) tensile strength and the toughness of GO films.[44] (b) Tensile strength and Young's modulus of MXene films.[106] (c) Fracture strain of GO films[44] and MXene films.[106] (d) Strength and the modulus of GO films as a function of the film's thickness. Reproduced with permission.[127] Copyright © 2019, Published by Elsevier Ltd. (e1) Tensile strength and Young's modulus of MXene films. (e2) Stress–strain curves of GO films with different thicknesses. Reproduced with permission.[132] Copyright © 2023, the American Chemical Society.

Table 5 Effect of film's thickness on the mechanical properties of the 2D material films

2D Material	Fabrication technique	Film thickness (μm)	Tensile strength (MPa)	Young's modulus (GPa)	Toughness (MJ m^{-3})	Strain to failure (%)	Ref.
GO	VAF	35	~33	~19	—	~0.135	127
		86	~23	~17.5	—	~0.15	
		138	~20.5	~10	—	~0.15	
$Ti_3C_2T_x$	VAF	2.3	61 ± 14	17 ± 4	—	0.89 ± 0.40	106
		4.5	~57 ± 14	~16 ± 4	—	—	
		7.7	~42.5 ± 7	~11.5 ± 4	—	—	
		17	36 ± 5	8 ± 2	—	—	
$Ti_3C_2T_x$	Blade coating	~0.94	568 ± 24	20.6 ± 3.1	3.0 ± 0.3	3.2 ± 0.2	143
		~2.4	480 ± 35	18.3 ± 2.8	8.4 ± 0.6	3.0 ± 0.3	
GO	Casting	4.9	59.6 ± 16	—	0.78 ± 0.17	3.2 ± 0.6	44
		7.6	78.5 ± 7.7	—	1.66 ± 0.19	3.9 ± 0.3	
		10.5	62.6 ± 5.3	—	2.12 ± 0.41	4.2 ± 0.5	
		12.5	84.5 ± 9.8	—	4.37 ± 0.94	9.8 ± 1.9	
		13.8	71.2 ± 11	—	3.46 ± 0.73	8.2 ± 0.7	
		15.7	70.8 ± 5.1	—	3.23 ± 0.53	7.0 ± 0.5	

Similarly, film thickness has a profound influence on the tensile strength, Young's modulus, and strain, which is enhanced by reducing the thickness, as shown in Fig. 7e. Table 5 presents the mechanical properties of various 2D material films in terms of film thickness. It is clear that most 2D material films exhibit the same trend regardless of the film's fabrication technique.

Fig. 8a and b presents a summary of the mechanical properties of various 2D materials in terms of material type, film thickness, and fabrication technique.

4.5. Post-processing

Post-processing of fabricated thin films, composed of 2D materials, offers additional prospects to define not only the mechanical properties but also the electrical conductivity, thermal conductivity,[175] optoelectronic properties,[176] and EMI shielding performance.[177] Chemical or thermal treatment of the films can modulate the water content, interlayer bridging, and porosity level. Thermal annealing and densification processes (Fig. 9) are discussed as post-processing approaches in the subsequent section.

4.5.1. Annealing treatment. The intrinsic mechanical properties of the 2D material films can be modulated by annealing. Thermal annealing modifies the characteristics of the interlayer spacing between adjacent nanoflakes. For instance, it regulates the water content within the film, which defines, to a certain extent, the mechanical properties. The water molecules introduced within the interlayer spacing between nanosheets weaken the intensity of interactions between

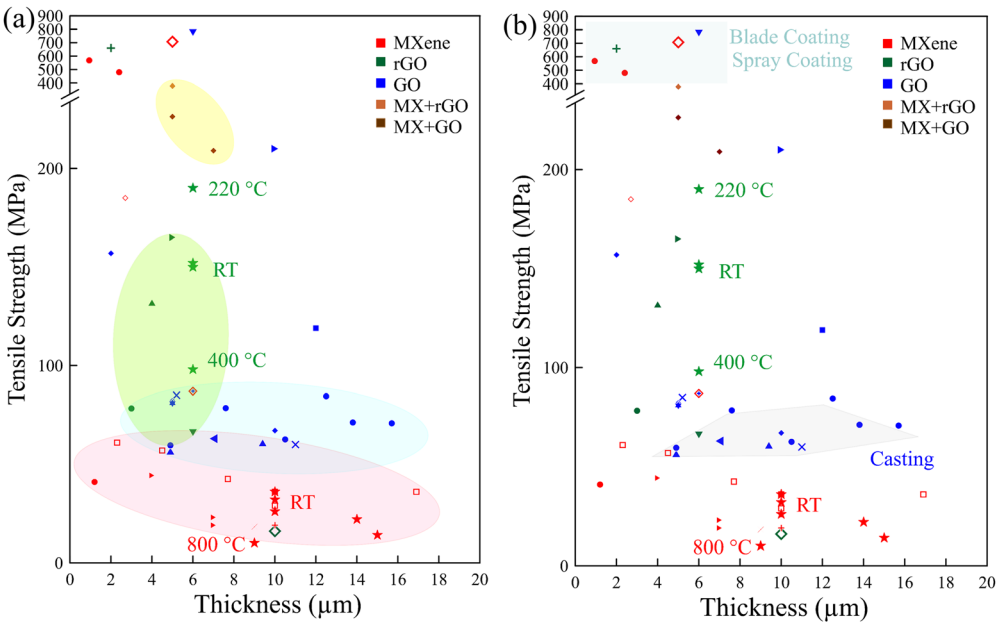

Fig. 8 Summary of (a) film thickness-dependent mechanical properties. (b) Fabrication technique-dependent mechanical properties. Most of the data were obtained at room temperature (RT); some were obtained at increased temperature, annotated in the figure. The data shown in this figure are presented in Table 2.

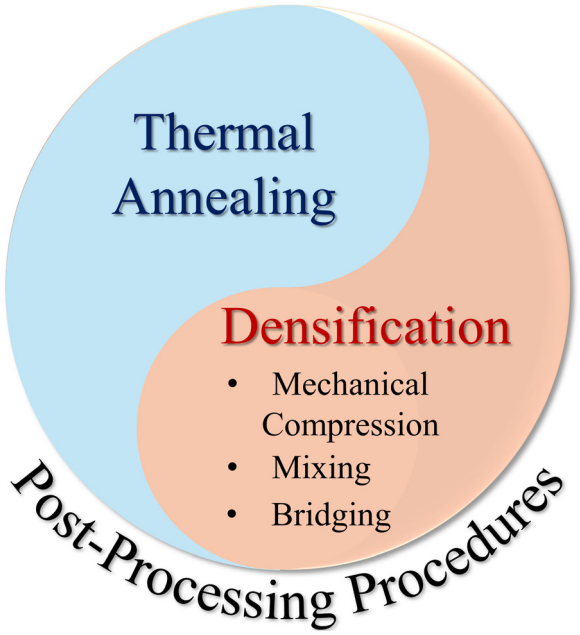

Fig. 9 Post-processing procedures discussed in this review.

individual flakes, which makes a major contribution to mechanical properties. Furthermore, the applied annealing temperature can influence the intensity of functional groups and the degree of oxidation,[178,179] which significantly impacts the inherent deformation of flakes.

Frequently, 2D material films were heated to a moderate temperature after fabrication to adjust the moisture content. However, the thermal treatment of such films at elevated temperatures was found to affect their mechanical performance. Dikin *et al.*[109] demonstrated that for GO films, there is a jump in both the elastic modulus from 17 to 25 GPa and the tensile strength from 45 to 135 MPa when the films were tested at 40 °C and 120 °C, respectively. The water-related characteristics of GO films are akin to cellulose-based films, in which dry films have higher strength and stiffness compared to wet films.[180] Moreover, the flexural strength of GO films is sensitive to the annealing temperature and duration.[127] The flexural strength was found to increase with higher temperature, peaking at about 105 MPa, when annealed at 150 °C for two hours. However, annealing GO films at 200 °C caused significant deterioration of flexural strength to about 25 MPa. Furthermore, the annealing duration at 100 °C was found to be optimal at 120 minutes.

Similarly, the mechanical properties of thermally annealed rGO films were found to surpass those dried at room temperature.[107] The tensile test results demonstrate a thermal annealing effect, which modifies the stiffness and strength of rGO films. As presented in Fig. 10b, both stiffness and strength increase with higher annealing temperatures, peaking at around 220 °C. Annealing the films at 220 °C results in the highest average Young's modulus, reaching 41.8 GPa, and the highest average tensile strength, reaching 293.3 MPa. However, when the annealing treatment was carried out at temperatures exceeding 220 °C, the graphene paper was more brittle, leading to a decline in both measured stiffness and strength as the annealing temperature increased. Additionally, it was demonstrated that rGO films that were dried at room temperature exhibited both elastic and plastic deformation regions, along with an initial straightening region. However, at annealing temperatures exceeding 100 °C, the plastic deformation becomes difficult to observe.

Annealing treatment was endorsed as an effective approach to thermally reduce GO into rGO.[182] Thermally reducing GO films to obtain rGO films resulted in lower tensile strength compared to GO films before graphitization at 2600 °C.[173] However, for rGO films annealed from 1300 to 1700 °C, those treated at 1500 °C demonstrate optimized mechanical performance,[181] as shown in Fig. 10c. Peng *et al.*[129] demonstrated that thermally treating rGO films at 3000 °C after reduction at 1300 °C yielded a modified tensile strength and fracture strain. Similarly, hot pressing of GO films at 2000 °C produces rGO films with modified mechanical properties.[131] In contrast, Xin *et al.*[126] proved that thermal treatment of rGO films at 2850 °C deteriorates both the tensile strength and Young's modulus by 11.8% and 56%, respectively. However, the tensile failure strain increases by about 40%, as shown in Fig. 10g.

David and Singh[112] investigated systematically the effect of graphitization temperature, ranging from 300 to 900 °C, to obtain robust rGO films. SEM images of the rGO film's cross-sections (Fig. 11a) disclose that the higher the annealing temperature, the more disordered the structure obtained. This structural alteration is linked to the progressive removal of oxygen groups, leading to a defective graphitic plane.[183] This increased irregularity of individual graphene nanosheets gave the papers a fluffier appearance. Additionally, the thickness expanded from 10 μm to 15 μm for films annealed at 300 °C and 900 °C (labeled 300 rGO and 900 rGO), respectively. Accordingly, as the annealing temperature increased, both the tensile strength and the failure strain deteriorated to lower values, and the rGO films exhibited more brittle behavior, as shown in Fig. 11b. Compared to chemically reduced rGO films,[107,183] thermally reduced films exhibit lower strength and higher strain to failure. This is due to the random-oriented and highly crumpled flakes, which allow for considerable straightening and unfolding actions. The successful oxidation of graphite to GO, followed by its subsequent thermal reduction to rGO, was verified using Raman, XRD, and XPS techniques. Fig. 11c displays the Raman spectrum, indicating the typical G-peak and the emergence of the D-peak in both the GO and rGO papers. Notably, no significant change is observed in the peak position with varying annealing temperatures. XRD patterns reveal a substantial increase in interlayer spacing between graphite, exhibiting its characteristic peak at $2\theta = 26.55°$, which corresponds to a *d*-spacing of ~3.4 Å, and GO at $2\theta = 11°$ (with a d-spacing of ~8.01 Å) due to extensive functionalization. As a result of the removal of oxygen groups during thermal reduction, the interlayer spacing of rGO gradually approached that of graphite. Additionally, peak broadening is noted, suggesting a wide distribution of graphene interlayer spaces within the paper.[112] X-ray photoelectron spectroscopy (XPS) was

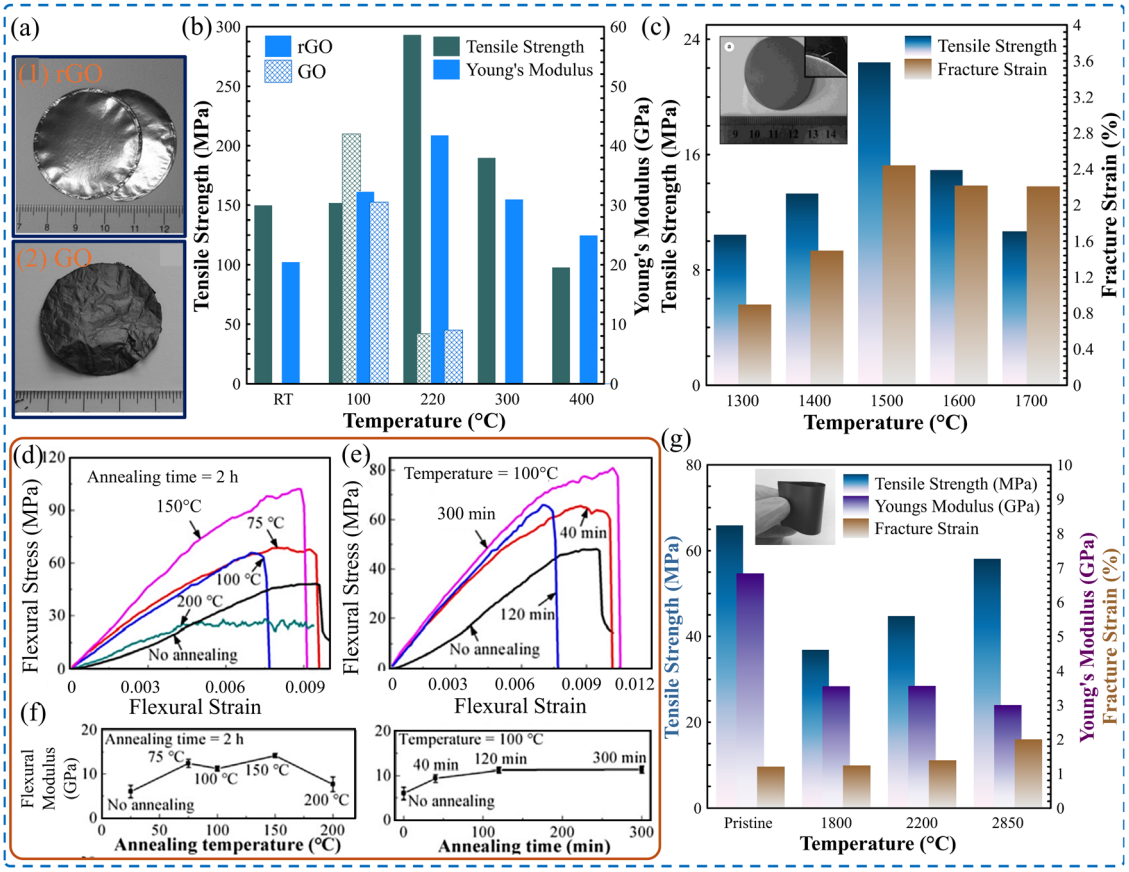

Fig. 10 (a) Image of (1) rGO film, and (2) GO film. (b) Tensile strength and Young's modulus of GO and rGO annealed at various temperatures. Reproduced with permission.[107] Copyright © 2008, WILEY-VCH Verlag GmbH & Co. KGaA, Weinheim. (c) Tensile strength and fracture strain of rGO films at different graphitization temperatures (inset: digital image of rGO film). Reproduced with permission.[181] Copyright © 2017, Institute of Coal Chemistry, Chinese Academy of Sciences. Published by Elsevier B.V. (d)–(f) Flexural strength and flexural modulus of GO films as a function of annealing temperature and duration. Reproduced with permission.[127] Copyright © 2019 Published by Elsevier Ltd. (g) Effect of annealing temperature on the mechanical properties of rGO films (inset: digital image of graphene film). Reproduced with permission.[126] Copyright © 2014, WILEY-VCH Verlag GmbH & Co. KGaA, Weinheim.

employed for the chemical analysis of thermal rGO by examining the C 1s peak (Fig. 11d). There is a reduction in the CO peak intensity, accompanied by a narrowing of the graphitic carbon and epoxy/ether carbon peaks as the annealing temperature increases. Similarly, the oxygen percentage (O 1s) decreases from 15.41 to 10.71 atom % with the elevation of the annealing temperature from 300 to 900 °C. The effect of annealing temperature on the mechanical properties of 2D material films is summarized in Table 6.

The annealing process was exploited to obtain mechanically robust $Ti_3C_2T_x$ MXene structures and concomitantly maintain its electrochemical performance. Annealing $Ti_3C_2T_x$ MXene films fabricated *via* the VAF process at high temperatures (500 and 650 °C) for one hour caused a reduction in their tensile strength from 36 MPa to 32 MPa and 26 MPa, respectively.[146] However, the annealed $Ti_3C_2T_x$ MXene films retained the outstanding flexibility that allowed them to be bent freely without any noticeable damage, as shown in Fig. 12a and b. It was proven that the amount of interlayer functional groups (–F and –O) and the corresponding interlayer spacing can be impacted by the annealing temperature, as shown in Fig. 12c and d. Thus, the overall mechanical properties are improved by the enhanced interactions between individual nanoflakes. Evidently, the chemical composition detected by XPS indicates that the amount of the –F terminal group deteriorates after annealing at high temperatures for a long time; they almost disappear at 800 °C, as shown in Fig. 12e. Additionally, the shifts of the peak of the (002) plane obtained by XRD show that the interlayer d-spacing decreases at elevated temperatures due to the loss of functional groups, as presented in Fig. 12f. Table 7 demonstrates the effect of annealing temperature on the mechanical properties, degree of oxidation, amount of –F terminal group, and interlayer *d*-spacing of MXene films.

4.5.2. Densification. The densification of 2D material films is another approach to obtaining highly compacted structures with enhanced mechanical performance by attenuation of void effects and by introducing bonding between adjacent flakes. Around a dozen methods, such as void elimination, mixing, and bridging, are grouped under this category. The elimination of voids between neighboring flakes, either *via* mechanical

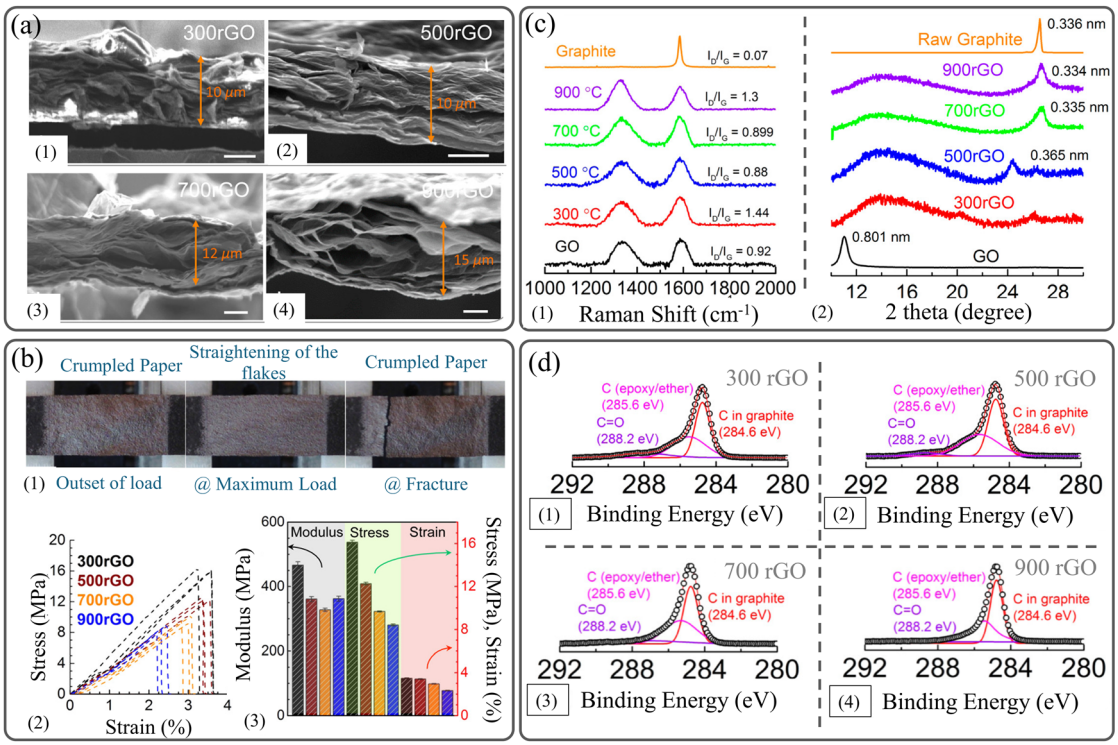

Fig. 11 (a) SEM images showing the effect of preparation temperature on the thickness of rGO films. (b) Mechanical properties of rGO films prepared at various temperatures. (c) Raman spectra and XRD patterns of rGO prepared at various temperatures. (d) XPS of rGO prepared at different temperatures. Reproduced with permission.[112] Copyright © 2014, American Chemical Society.

Table 6 Effect of annealing temperature on the mechanical properties of 2D material films

2D material	Fabrication technique	Film thickness (μm)	Temp. (°C)	Young's modulus (GPa)	Tensile strength (MPa)	Strain to failure (%)	Ref.
GO	VAF	11	120	25	135	—	109
GO	VAF	86	150	~14 (~115%)	~105[a] (~100%)	~0.9	127
rGO	VAF	6	220	41.8 (104%)	293.3 (96%)	~0.82	107
rGO	VAF	10	300	~0.47	~16	~3.5	112
rGO	Blade coating	14	2600	—	~43	7.85	173
rGO	VAF	—	1500	—	22.41	2.4	181
rGO	Blade coating	—	3000	—	~57	~16	129
rGO	Blade coating	13	2000	10	103.2	2.18	131
rGO	CCC	—	120	—	296 (~90%)	~2.75	125
rGO	Electro-spray deposition		2850	2	58.2	~2	126
$Ti_3C_2T_x$	VAF	10	—	—	36	~1.5	146

[a] Indicates results that were obtained from flexural tests.

compression or packing with bridging agents, can drastically control the mechanical properties of these materials. 2D material structures can be densified by mixing various types of 2D materials with controlled flake sizes.[124] For instance, $MoS_2/Ti_3C_2T_x$ hybrid films can fulfill a low porosity level and a high density ~2.9 g cm^{-3} without sacrificing the other properties.[185] Densification of MXene films *via* insertion of GO nanosheets endows the MXene/GO films with extraordinary electrical conductivity and EMI shielding performance.[186,187] Additionally, liquid-mediated densified holey MXene film can significantly increase the capacitance of the thin films by enhancing the ionic transport at 10 V s^{-1} to 1274 F cm^{-3}.[188] Moreover, densified films of MXene up to 40 times compared to the original state can show a capacitance of 1.4 F cm^{-2}.[2]

Moreover, bridging-induced densification of MXene films can be achieved *via* three methods: sequentially bridged MXene (SBM), hydrogen-bonded MXene (HBM), and covalently bridged MXene (CBM).[189] Film fabrication methods, such as SBM, ramp up the mechanical strength up to six orders of magnitude compared to conventional MXene film. MXene films fabricated by SBM can sustain up to one million cycles before failure at a stress level of about 500 MPa. The HBM and CBM can only hold one order of magnitude less than the SBM for a maximum of hundreds of thousands.

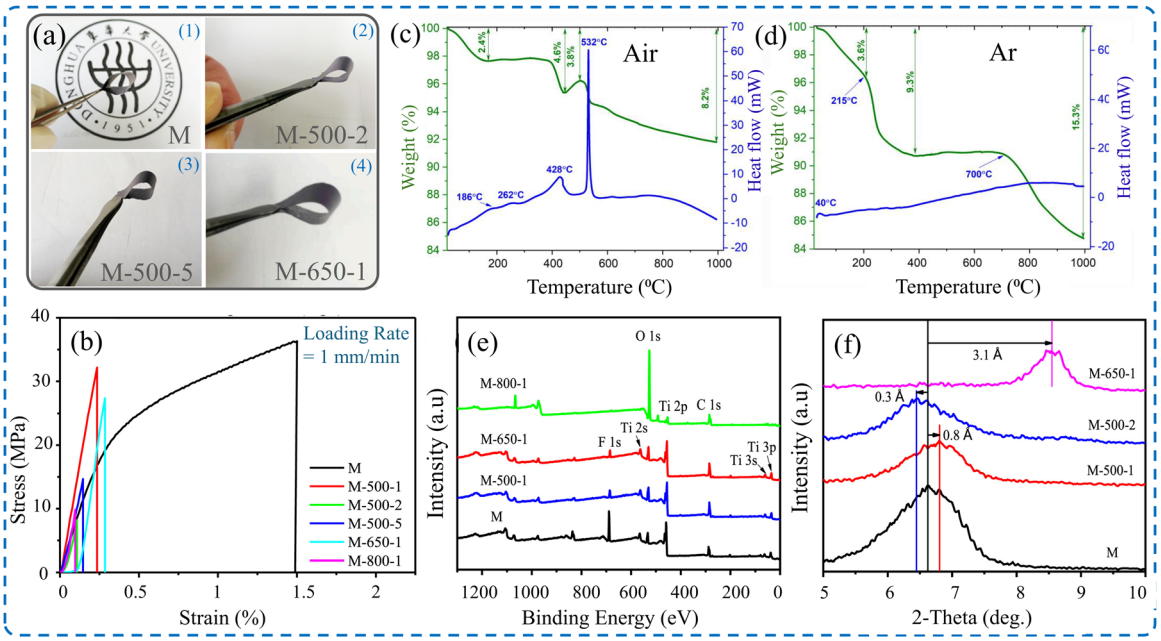

Fig. 12 (a) Digital image of flexible $Ti_3C_2T_x$ MXene films treated at different temperatures.[146] (b) Stress–strain curves of $Ti_3C_2T_x$ MXene films showing the effect of annealing temperature and duration. TGA and DSC curves of $Ti_3C_2T_x$ MXene films under (c) air atmosphere and (d) argon atmosphere.[184] (e) X-ray photoelectron spectrum of MXene films after annealing at different temperatures and durations. (f) X-ray diffraction patterns of MXene films after annealing at different temperatures and durations. Reproduced with permission.[146] Copyrights © 2020, Elsevier B.V.

Table 7 Effect of annealing temperature on the mechanical properties, degree of oxidation, amount of –F– terminal group, and interlayer *d*-spacing of MXene films[146]

Annealing temperature (°C)	Annealing duration (h)	Film thickness (μm)	Areal density (gm cm^{-2})	Tensile strength (MPa)	Failure strain (%)	Degree of oxidation (%)	F 1s (%)	*d*-Spacing (Å)
—	—	10	3	36	~1.5	0.8	25.6	13.4
500	1	10	3.7	32	~0.25	3.4	8.2	12.6
	2	14	3.2	22	~0.125	10.2	1.89	13.7
	5	15	2.7	14	~0.18	15.3	1.71	—
650	1	10	3.7	26	~0.3	3.6	6.72	10.3
800	1	9	3.4	10	~0.12	17.6	1.45	—

Atomic force microscopy was used to densify the carbon nanotube (CNT) films. Through repetitive indentation, the film sheets collapsed on each other, forming a stiff network that could resist higher stresses compared to the pristine CNT films. The film's Young's modulus increased with the number of indentations because of the entanglement of the densified film, which bore more plasticity compared to the intact films.[190]

Molding was used to stack 2D sheets into 3D configurations after exfoliation, as shown in Fig. 13a.[191] Consequently, such structures enhance the mechanical strength of the 2D materials by bearing extra loads, boosting their Young's modulus, as illustrated in Fig. 13b–f. 3D structures can also benefit from the effect of densification; for example, the densification of graphene foams leads to increased Young's modulus and tensile strength.[192] Henceforth, 2D materials exfoliated from TMDs, specifically molybdenum disulfide (MoS_2) densified films, have superior conductivity over their conventional counterparts. Such MoS_2 films exhibit high conductivity at 47 S cm^{-1}, which is 108% higher than that of non-densified films.[185] In addition, carrier concentration increased when MoS_2 thin films were synthesized using CVD with nitrogen gas, hence increasing the conductivity of the as-produced films.[193] By increasing the number of deposited layers, the sheet resistance of graphene thin film decreases, and the self-assembly densification technique reduces the sheet resistance further by increasing the annealing temperature. In addition, more layers blocked visible light transmittance, making the material opaque.[194]

Within the same scope, thin films of graphene nanoplatelets (GNP) were densified by 196% using a hydraulic method.[196] Coupling graphene with waterborne polyurethane (WPU) yielded an electrical conductivity of 1004.4 S m^{-1}, which was 26% higher than the non-densified films. The mechanical strength reached about 48.5 MPa at a failure strain of 5% for the lowest concentration.[197] Highly densified MXene films can have a strength of 570 MPa for a thickness of 940 nm, an enhancement of 134% from the densified by intercalation films, coupled with an electrical conductivity of 15 100 S cm^{-1}.[143] With the intercalation between the layers of the conventional MXene

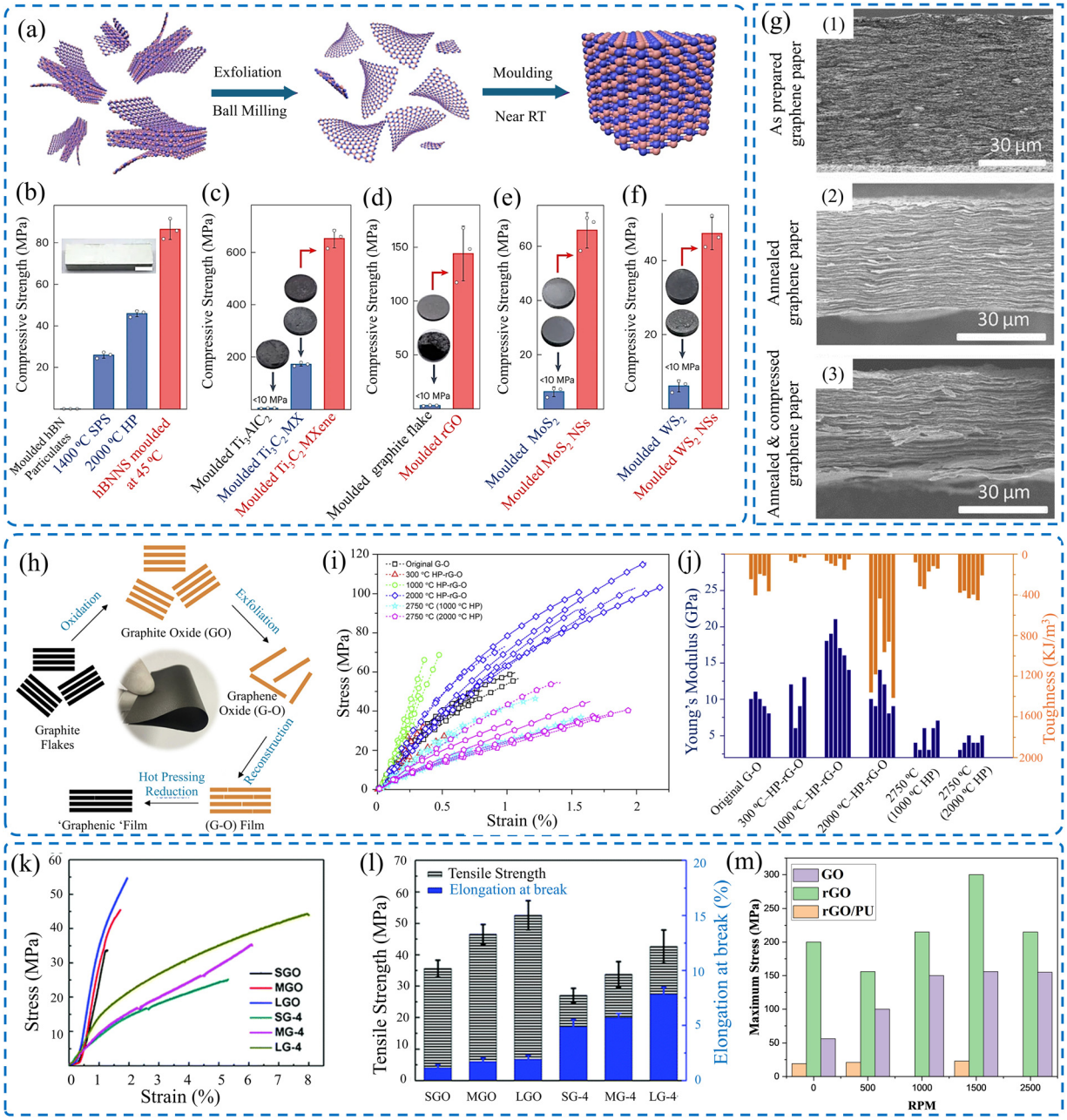

Fig. 13 (a) Molding of exfoliated 3D structures out of 2D sheets. Mechanical proprieties of molded (b) hBN, (c) MXene, (d) rGO, (e) MoS_2, and (f) WS_2. Reproduced with permission.[191] Copyright © 2024, Springer Nature Limited. (g) SEM images of (1) as-prepared graphene paper, (2) annealed graphene paper, and (3) post-annealing compression of graphene paper. Reproduced with permission.[195] Copyrights © 2017, WILEY-VCH Verlag GmbH & Co. KGaA, Weinheim. (h) Scheme of the fabrication of the graphenic film. Effect of hot pressing on the (i) tensile strength, and (j) Young's modulus and toughness of rGO films. Reproduced with permission.[131] Copyrights © 2018, Elsevier Ltd. (k) Stress–strain curves of treated GO films. (l) Effect of annealing, followed by compression on the tensile strength and elongation of GO films.[173] (m) Tensile strength in terms of rotating speed of GO, rGO, and rGO/PU made by centrifugal continuous casting process.[125]

films, Jang *et al.*[198] used polyaniline (PANI) as an intercalation agent to densify MXene films. Such films have a higher strength than conventional films by almost 10 MPa more. Wood, as a natural biodegradable source, can be used as a substrate for thin films using delignification. Using a hot-pressing method, the infused wood with MXene densified thin film has a Young's modulus of 14.6 GPa and a tensile strength of 424.7 MPa.[199]

Gelation is yet another assisting method used to densify MXene thin films. When doing so, the fabricated MXene sheets are trapped in highly viscous gels. The gels with MXene nanosheets are placed under high rolling pressure, aligning the MXene sheets on top of each other and fabricating films that are densified when squeezed.[200] The films show 286 MPa of strength with a failure strain of up to 6%. Similarly, the

continuous centrifugal casting (CCC) technique was used to densify rGO films, increasing their mechanical strength, Young's modulus, and electrical conductivity. In this technique, the high-speed centrifugal process induced a high force that aligned the rGO sheets well, reinforcing the structure. Consequently, the compacting stress increased as the revolution per minute increased.[125] It is evident from Fig. 13m that as the speed of the spin coater increases, the thin film across all the materials experiences higher stress; hence, their tensile strength increases.

In more chemically oriented methods, intercalation of 2D materials with atoms, ions, or molecules can induce modified mechanical properties by enhancing interlayer interactions.[201] For instance, it was shown that the interlayer characteristics, such as resistivity, between adjacent MXene flakes highly depended on the intercalated cation. Whether its K^+, Cs^+, Na^+, Li^+, or Mg^{2+}, each cation intercalated can affect the density of the layers of the thin film, hence changing the resistivity with an inverse or proportional effect.[202,203] Additionally, thin films densified by intercalation can experience a tensile strength of 112 MPa and 4% failure strain.[204]

A novel method of ball milling, followed by VAF, is imposed to stack 2D graphene sheets, followed by annealing and compression to further increase the electrical conductivity of the thin films, as shown in Fig. 13g.[195] Additionally, thermal annealing accompanied by mechanical pressing has proven to be an effective approach for modifying the mechanical properties of rGO films, as shown in Fig. 13h–j.[131] Such a method increases the mechanical strength of the film to at least double the non-densified one.

Films densified by hot rolling possess yet another advantage over non-densified films.[134] The hot-rolled rGO films were not only stronger but also more flexible with folding possibilities. Moreover, it was noted that chemically modified GO films exhibited a significant improvement in mechanical properties and fracture strength. This modification can be achieved by importing a small amount (less than 1 wt%) of Mg^{2+} and Ca^{2+}.[134] The mechanical properties of densified rGO films *via* mechanical compression were investigated.[173] It demonstrated that, regardless of flake size, mechanically compressed rGO films have enhanced mechanical performance, as shown in Fig. 13l and m. Table 8 shows different parameters, such as strength and Young's modulus, for different 2D materials fabricated using different methods.

4.6. Effect of strain rate

As discussed earlier, the mechanical properties of 2D material films depend on the geometry, such as the thickness of the samples. The testing conditions, such as strain rate, were found to have a substantial impact on the mechanical properties.[32] However, gauge length was observed to have a trivial effect on the acquired tensile strength of $Ti_3C_2T_x$ MXene films,[106] and GO films.[149] This phenomenon is known for macroscopic films and individual nanoflakes. The deformation of 2D material nanoflakes exhibits sensitivity toward the applied strain rate demonstrated in previous studies for graphene,[206] h-BN,[207] borophene,[208] phosphorene,[209] silicin,[210] and MXenes.[211,212] 2D material films constructed by stacking layers in which the interlayer characteristics, such as functional groups and interactions between them, define the shear slippage between individual flakes. The mechanical behavior of such structures is sensitive to the loading conditions. The mechanical properties of the GO film strongly depended on the strain rate, where

Table 8 Effect of mechanical densification on the mechanical performance of 2D material films

2D Material	Densification stress (MPa)	Strength (MPa)	Enhancement of strength (%)	Young's modulus (GPa)	Failure strain (%)	Densification technique	Ref.
MXene	—	436	600	6.1	4.5	Bridging	189
MXene	1	908.4	520.5	56.6	2.1	Bridging + hot pressing	142
hBN	375	~86.4	230	~12.4	—	Molding	191
MXene	375	~652	116.5	—	—	Molding	191
rGO	375	~143	40	—	—	Molding	191
MoS_2	375	~65	147	—	—	Molding	191
WS_2	375	~48	131	—	—	Molding	191
Graphene	200	50.4	163.6	13	4	Hot pressing	192
Graphene	—	48.5	—	0.2	—	Blade coating	197
MXene	—	570	134	20.6	3.2	Blade coating	143
MXene	—	112	72	—	3.8	Liquid phase intercalation	204
MXene	—	47	25	—	3.5	Liquid intercalation	198
MXene	—	14 600	—	0.4247	3	Hot pressing	199
MXene	—	286	127.3	9.2	3.7	Rolling	200
rGO	—	660	106	—	—	CCC	125
rGO	—	41	—	5	2	Thermal annealing	201
rGO	—	16.7	150	0.32	9	Hot rolling	131
GO	—	16	40	16	0.6	Liquid intercalation	134
GO	300	42.6	—	—	15	Compression	173
MXene + GO	—	226.3	175.3	—	4.4	Mixing	123
MXene + rGO	—	379.2	128.7	—	7.2	Mixing	123
MXene + GO	—	209	809		~1.35	Mixing	130
rGO/MoS_2	—	9.48	−25	427.03	2.22	Mixing	205
MXene + GO	—	651.9	285	37.6	2.1	Mixing	124
MXene + rGO	—	864.3	181	31.6	3.5	Mixing	124
MXene + rGO	—	1871	507.8	98.7	2.4	Mixing + bridging	124

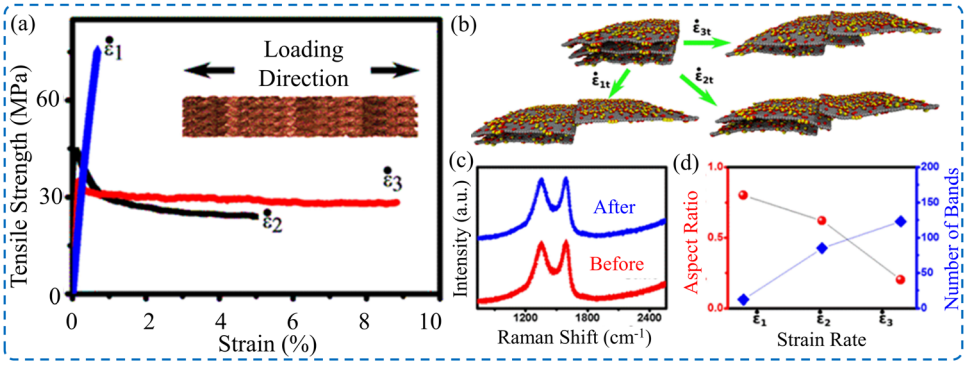

Fig. 14 (a) Stress–strain curves of GO film at various strain rates. (b) Images of molecular dynamic simulation results showing the relative sliding of layers at different strain rates. (c) Raman spectra of GO films before and after testing. (d) Number of deformation bands as a function of the applied strain rate. Reproduced with permission.[213] Copyright © 2016, the American Chemical Society.

the deformation exhibited brittle to ductile transition when the applied strain rate was reduced.[213] The tensile strength decreased from 85 to 50 MPa by reducing the strain rate from 0.1% min^{-1} to 0.01% min^{-1}, respectively. Additionally, there is a drastic increase in fracture strain from 0.1 to 9% for 0.1% min^{-1} to 0.01% min^{-1}, respectively, as presented in Fig. 14a. Although the deformation of individual flakes is sensitive to the straining rate, Raman spectra captured before and after testing (Fig. 14c) do not show permanent deformation of individual GO flakes. The MD simulation (Fig. 14b–d) showed that the higher the strain rates, the lower the transferred loads from the upper layer and the lower layer of a film. Thus, noticeable sliding of the upper layer and a lower number of deformation bands were observed. Despite these results, studies on the effect of strain rate on the mechanical deformation of 2D material films are still limited. Thus, more investigation is needed. Gao *et al.*[149] reported a strain rate effect, ranging from 10^{-4} to 10^{-2} s^{-1}, on the mechanical properties of GO films. The tensile test measurements show that the tensile strength and strain to failure for 10^{-2} s^{-1} increased by 135.2% and 115.1%, respectively, compared to the low strain rate of 10^{-4} s^{-1}.

5. Conclusion

This work introduces a comprehensive review of the mechanical deformation of 2D material films. Stress–strain curves of 2D material films made of GO, rGO, and MXenes are found to have similar behavior. Straightening of wrinkling, slippage, and pullouts was observed during the tensile testing of the films. Generally, the failure of films is initiated at critical defects and voids between flakes, which consequently act as a pre-crack for rapid crack propagation. Although brittle fracture is the most dominant and common behavior of the fracturing of such thin films, its mechanical properties are inconsistent and poorly reproducible. This is because of the dependence of mechanical properties on several factors, such as synthesis methods, size of monolayers, fabrication technique of the film, film's thickness, post-processing, and loading conditions. These parameters have substantial influences on the alignment of the nanoflakes, the level of defects, and the interlayer characteristics, which have a major contribution to define the mechanical properties of the films. The flake lateral size was found to have a profound impact on the mechanical performance of the films. The larger the flake size, the more enhanced the mechanical properties of the films. Regarding the fabrication technique of the films, VAF and drop casting techniques induced films with relatively low mechanical properties. However, optimized blade coating and controlled spray coating techniques produced ultra-strong thin films with enhanced mechanical performance. The mechanical property measurements revealed the film's thickness effect. Thinner films manifest higher properties, while the mechanical properties deteriorate for thicker films. Additionally, post-processing has a direct influence on mechanical properties. Thermal annealing and densification procedures yielded enhanced mechanical properties and fracture behavior of the treated films.

Data availability

No primary research results, software or code are included and no new data were generated or analyzed as part of this review.

Conflicts of interest

The authors declare no interest conflict. They have no known competing financial interests or personal relationships that could have appeared to influence the work reported in this paper.

Acknowledgements

The authors acknowledge the support provided by the Research & Innovation Center for Graphene and 2D Materials (RIC-2D) of Khalifa University under Award No. DP4-8434000508.

References

1 W. Wei, M. Zhang, J. Ren and K. Wang, *ACS Appl. Nano Mater.*, 2024, 7, 14844–14864.

2 D. Spurling, H. Krüger, N. Kohlmann, F. Rasch, M. P. Kremer, L. Kienle, R. Adelung, V. Nicolosi and F. Schütt, *Energy Storage Mater.*, 2024, **65**, 103148.
3 N. Thakur, P. Kumar, S. Kumar, A. K. Singh, H. Sharma, N. Thakur, A. Dahshan and P. Sharma, *Prog. Solid State Chem.*, 2024, **74**, 100443.
4 J. T. Kim, C. W. Lee, H. J. Jung, H. J. Choi, A. Salman, S. Padmajan Sasikala and S. O. Kim, *ACS Nano*, 2022, **16**, 17687–17707.
5 D. Berman, L. I. Farfan-Cabrera, A. Rosenkranz and A. Erdemir, *Nat. Rev. Mater.*, 2024, **9**, 527–529.
6 K. Ledwaba, S. Karimzadeh and T. C. Jen, *Mater. Today Sustainability*, 2023, **22**, 100412.
7 Y.-C. Lin, R. Torsi, R. Younas, C. L. Hinkle, A. F. Rigosi, H. M. Hill, K. Zhang, S. Huang, C. E. Shuck, C. Chen, Y.-H. Lin, D. Maldonado-Lopez, J. L. Mendoza-Cortes, J. Ferrier, S. Kar, N. Nayir, S. Rajabpour, A. C. T. van Duin, X. Liu, D. Jariwala, J. Jiang, J. Shi, W. Mortelmans, R. Jaramillo, J. M. J. Lopes, R. Engel-Herbert, A. Trofe, T. Ignatova, S. H. Lee, Z. Mao, L. Damian, Y. Wang, M. A. Steves, K. L. Knappenberger, Jr., Z. Wang, S. Law, G. Bepete, D. Zhou, J.-X. Lin, M. S. Scheurer, J. Li, P. Wang, G. Yu, S. Wu, D. Akinwande, J. M. Redwing, M. Terrones and J. A. Robinson, *ACS Nano*, 2023, **17**, 9694–9747.
8 A. K. Katiyar, A. T. Hoang, D. Xu, J. Hong, B. J. Kim, S. Ji and J.-H. Ahn, *Chem. Rev.*, 2024, **124**, 318–419.
9 W. Yu, K. Gong, Y. Li, B. Ding, L. Li, Y. Xu, R. Wang, L. Li, G. Zhang and S. Lin, *Small*, 2022, **18**, 2105383.
10 V. Chaudhary, A. Kaushik, H. Furukawa and A. J. E. S. P. Khosla, *ECS Sens. Plus*, 2022, **1**, 013601.
11 J. Wait, G. Josephson, B. C. Wyatt, B. Anasori and A. Çolak, *Carbon*, 2023, **213**, 118284.
12 H. Jiang, L. Zheng, Z. Liu and X. J. I. Wang, *InfoMat*, 2020, **2**, 1077–1094.
13 J. H. Kim, J. H. Jeong, N. Kim, R. Joshi and G.-H. Lee, *J. Phys. D: Appl. Phys.*, 2018, **52**, 083001.
14 D. Akinwande, C. J. Brennan, J. S. Bunch, P. Egberts, J. R. Felts, H. Gao, R. Huang, J.-S. Kim, T. Li and Y. Li, *Extreme Mech. Lett.*, 2017, **13**, 42–77.
15 K. Liu and J. J. J. o M. R. Wu, *J. Mater. Res.*, 2016, **31**, 832–844.
16 A. Lipatov, H. Lu, M. Alhabeb, B. Anasori, A. Gruverman, Y. Gogotsi and A. Sinitskii, *Sci. Adv.*, 2018, **4**, eaat0491.
17 S. J. Lee, S. J. Yoon and I.-Y. J. P. Jeon, *Polymers*, 2022, **14**, 4733.
18 A. Kamal, M. Ashmawy, A. M. Algazzar and A. H. Elsheikh, *Proc. Inst. Mech. Eng., Part C*, 2022, **236**, 4843–4861.
19 M. Y. Khalid, A. Kamal, A. Otabil, O. Mamoun and K. Liao, *Chem. Eng. J. Adv.*, 2023, **16**, 100537.
20 Y.-Q. Li, T. Yu, T.-Y. Yang, L.-X. Zheng and K. Liao, *Adv. Mater.*, 2012, **24**, 3426–3431.
21 Y. Xu, K. Sheng, C. Li and G. Shi, *ACS Nano*, 2010, **4**, 4324–4330.
22 L. Paliotta, G. De Bellis, A. Tamburrano, F. Marra, A. Rinaldi, S. Balijepalli, S. Kaciulis and M. J. C. Sarto, *Carbon*, 2015, **89**, 260–271.
23 P. Bhattacharya, D. Du and Y. Lin, *J. R. Soc., Interface*, 2014, **11**, 20131067.
24 P. Zhou, H. Yu, Y. Zhong, W. Zou, Z. Wang and L. Liu, *Nano-Micro Lett.*, 2020, **12**, 166.
25 G. Zan and Q. Wu, *Adv. Mater.*, 2016, **28**, 2099–2147.
26 J. Chen, Z. Li, F. Ni, W. Ouyang and X. Fang, *Mater. Horiz.*, 2020, **7**, 1828–1833.
27 S. Wan, L. Jiang and Q. Cheng, *Matter*, 2020, **3**, 696–707.
28 S. Iravani and R. S. Varma, *Mater. Adv.*, 2022, **3**, 4783–4796.
29 W. Cao, Z. Wang, X. Liu, Z. Zhou, Y. Zhang, S. He, D. Cui and F. Chen, *Nano-Micro Lett.*, 2022, **14**, 119.
30 A. Akbari, P. Sheath, S. T. Martin, D. B. Shinde, M. Shaibani, P. C. Banerjee, R. Tkacz, D. Bhattacharyya and M. Majumder, *Nat. Commun.*, 2016, **7**, 10891.
31 S. Wan, Y. Chen, Y. Wang, G. Li, G. Wang, L. Liu, J. Zhang, Y. Liu, Z. Xu, A. P. Tomsia, L. Jiang and Q. Cheng, *Matter*, 2019, **1**, 389–401.
32 A. R. Ranjbartoreh, B. Wang, X. Shen and G. Wang, *J. Appl. Phys.*, 2011, **109**, 014306.
33 T. Huang, B. Zheng, Z. Liu, L. Kou and C. Gao, *J. Mater. Chem. A*, 2015, **3**, 1890–1895.
34 G. Yang, H. Yi, Y. Yao, C. Li and Z. Li, *ACS Appl. Nano Mater.*, 2020, **3**, 2149–2155.
35 C. E. Shuck and Y. J. C. E. J. Gogotsi, *Chem. Eng. J.*, 2020, **401**, 125786.
36 K. Rasool, K. A. Mahmoud, D. J. Johnson, M. Helal, G. R. Berdiyorov and Y. Gogotsi, *Sci. Rep.*, 2017, **7**, 1598.
37 M. Shekhirev, J. Busa, C. E. Shuck, A. Torres, S. Bagheri, A. Sinitskii and Y. Gogotsi, *ACS Nano*, 2022, **16**, 13695–13703.
38 B. Wang, T. Szkopek and M. Cerruti, *Carbon*, 2022, **192**, 145–152.
39 R. Yang, X. Chen, Y. Zheng, K. Chen, W. Zeng and X. Wu, *J. Mater. Chem. C*, 2022, **10**, 5380–5399.
40 X. Lin, X. Shen, Q. Zheng, N. Yousefi, L. Ye, Y.-W. Mai and J.-K. Kim, *ACS Nano*, 2012, **6**, 10708–10719.
41 Z. Liu, Z. Li, Z. Xu, Z. Xia, X. Hu, L. Kou, L. Peng, Y. Wei and C. Gao, *Chem. Mater.*, 2014, **26**, 6786–6795.
42 J. Lipton, J. A. Röhr, V. Dang, A. Goad, K. Maleski, F. Lavini, M. Han, E. H. R. Tsai, G.-M. Weng, J. Kong, E. Riedo, Y. Gogotsi and A. D. Taylor, *Matter*, 2020, **3**, 546–557.
43 K. Hu, D. D. Kulkarni, I. Choi and V. V. Tsukruk, *Prog. Polym. Sci.*, 2014, **39**, 1934–1972.
44 S. Ye, B. Chen and J. Feng, *Sci. Rep.*, 2015, **5**, 1–10.
45 N. R. Glavin, R. Rao, V. Varshney, E. Bianco, A. Apte, A. Roy, E. Ringe and P. M. Ajayan, *Adv. Mater.*, 2020, **32**, 1904302.
46 A. R. Urade, I. Lahiri and K. J. J. Suresh, *JOM*, 2023, **75**, 614–630.
47 D. J. D. Ayodhya, *Diamond Relat. Mater.*, 2022, **132**, 109634.
48 A. VahidMohammadi, J. Rosen and Y. Gogotsi, *Science*, 2021, **372**, eabf1581.
49 K. S. Novoselov, A. K. Geim, S. V. Morozov, D.-E. Jiang, Y. Zhang, S. V. Dubonos, I. V. Grigorieva and A. Firsov, *Science*, 2004, **306**, 666–669.
50 H. Zhang, *ACS Nano*, 2015, **9**, 9451–9469.
51 F. Bechstedt, P. Gori and O. Pulci, *Prog. Surf. Sci.*, 2021, **96**, 100615.

52 L. Du, M. R. Molas, Z. Huang, G. Zhang, F. Wang and Z. Sun, *Science*, 2023, **379**, eadg0014.
53 A. K. J. s Geim, *Science*, 2009, **324**, 1530–1534.
54 O. Salim, K. Mahmoud, K. Pant and R. J. M. T. C. Joshi, *Mater. Today Chem.*, 2019, **14**, 100191.
55 Y. Shi, C. Hamsen, X. Jia, K. K. Kim, A. Reina, M. Hofmann, A. L. Hsu, K. Zhang, H. Li, Z.-Y. Juang, M. S. Dresselhaus, L.-J. Li and J. Kong, *Nano Lett.*, 2010, **10**, 4134–4139.
56 C. Ataca, H. Sahin and S. Ciraci, *J. Phys. Chem. C*, 2012, **116**, 8983–8999.
57 S. Manzeli, D. Ovchinnikov, D. Pasquier, O. V. Yazyev and A. Kis, *Nat. Rev. Mater.*, 2017, **2**, 17033.
58 H. Furukawa, K. E. Cordova, M. O'Keeffe and O. M. Yaghi, *Science*, 2013, **341**, 1230444.
59 T. Chen and D. Wang, in *Encyclopedia of Interfacial Chemistry*, ed. K. Wandelt, Elsevier, Oxford, 2018, pp. 446–452, DOI: 10.1016/B978-0-12-409547-2.13071-9.
60 P. S. Jijoe, S. R. Yashas and H. P. Shivaraju, *Environ. Chem. Lett.*, 2021, **19**, 2643–2661.
61 K. Zhou, G. Shang, H. H. Hsu, S. T. Han, V. A. Roy and Y. J. A. M. Zhou, *Adv. Mater.*, 2023, **35**, 2207774.
62 M. Dávila, L. Xian, S. Cahangirov, A. Rubio and G. Le Lay, *New J. Phys.*, 2014, **16**, 095002.
63 B. Lalmi, H. Oughaddou, H. Enriquez, A. Kara, S. Vizzini, B. Ealet and B. Aufray, *Appl. Phys. Lett.*, 2010, 97.
64 S. Rani, K. Suganthi and S. C. Roy, *J. Electron. Mater.*, 2023, **52**, 3563–3575.
65 M. G. Chaudhary, N. Kumar and S. Kumar, *Evergreen:Jt. J. Novel Carbon Resour. Sci. Green Asia Strategy*, 2021, **8**, 732–749.
66 H. Liu, A. T. Neal, Z. Zhu, Z. Luo, X. Xu, D. Tománek and P. D. Ye, *ACS Nano*, 2014, **8**, 4033–4041.
67 H. You, Y. Jia, Z. Wu, F. Wang, H. Huang and Y. Wang, *Nat. Commun.*, 2018, **9**, 2889.
68 A. Thakur and B. Anasori, *Science*, 2024, **383**, 1182–1183.
69 J. Björk, J. Zhou, P. O. Å. Persson and J. Rosen, *Science*, 2024, **383**, 1210–1215.
70 G. Wang, H. Hou, Y. Yan, R. Jagatramka, A. Shirsalimian, Y. Wang, B. Li, M. Daly and C. Cao, *Int. J. Extreme Manuf.*, 2023, **5**, 032002.
71 M. Galluzzi, Y. Zhang and X.-F. Yu, *J. Appl. Phys.*, 2020, **128**, 230903.
72 Y. Hou, J. Zhou, Z. He, J. Chen, M. Zhu, H. Wu and Y. Lu, *Nat. Commun.*, 2024, **15**, 4033.
73 Y. I. Jhon, Y. M. Jhon, G. Y. Yeom and M. S. J. C. Jhon, *Carbon*, 2014, **66**, 619–628.
74 M. Dewapriya and S. A. J. C. M. S. Meguid, *Comput. Mater. Sci.*, 2018, **141**, 114–121.
75 C. Daniels, A. Horning, A. Phillips, D. V. Massote, L. Liang, Z. Bullard, B. G. Sumpter and V. Meunier, *J. Phys.: Condens. Matter*, 2015, **27**, 373002.
76 X. Li, M. Sun, C. Shan, Q. Chen and X. Wei, *Adv. Mater. Interfaces*, 2018, **5**, 1701246.
77 S. Bertolazzi, J. Brivio and A. Kis, *ACS Nano*, 2011, **5**, 9703–9709.
78 A. Falin, Q. Cai, E. J. Santos, D. Scullion, D. Qian, R. Zhang, Z. Yang, S. Huang, K. Watanabe and T. Taniguchi, *Nat. Commun.*, 2017, **8**, 15815.
79 J. W. Suk, R. D. Piner, J. An and R. S. Ruoff, *ACS Nano*, 2010, **4**, 6557–6564.
80 C. Gómez-Navarro, M. Burghard and K. Kern, *Nano Lett.*, 2008, **8**, 2045–2049.
81 C. Lee, X. Wei, J. W. Kysar and J. Hone, *Science*, 2008, **321**, 385–388.
82 Y. Li, C. Wei, S. Huang, A. Ghasemi, W. Gao, C. Wu and V. N. Mochalin, *ACS Appl. Nano Mater.*, 2021, **4**, 5058–5067.
83 K. L. Firestein, J. E. von Treifeldt, D. G. Kvashnin, J. F. S. Fernando, C. Zhang, A. G. Kvashnin, E. V. Podryabinkin, A. V. Shapeev, D. P. Siriwardena, P. B. Sorokin and D. Golberg, *Nano Lett.*, 2020, **20**, 5900–5908.
84 B. Jang, A. E. Mag-isa, J.-H. Kim, B. Kim, H.-J. Lee, C.-S. Oh, T. Sumigawa and T. Kitamura, *Extreme Mech. Lett.*, 2017, **14**, 10–15.
85 G.-H. Lee, R. C. Cooper, S. J. An, S. Lee, A. Van Der Zande, N. Petrone, A. G. Hammerberg, C. Lee, B. Crawford and W. Oliver, *Science*, 2013, **340**, 1073–1076.
86 K. Cao, S. Feng, Y. Han, L. Gao, T. Hue Ly, Z. Xu and Y. Lu, *Nat. Commun.*, 2020, **11**, 284.
87 M. Annamalai, S. Mathew, M. Jamali, D. Zhan and M. Palaniapan, *J. Micromech. Microeng.*, 2012, **22**, 105024.
88 Y. Zhang and C. Pan, *Diamond Relat. Mater.*, 2012, **24**, 1–5.
89 I. Frank, D. M. Tanenbaum, A. M. van der Zande and P. L. McEuen, *J. Vac. Sci. Technol., B:Microelectron. Nanometer Struct.–Process., Meas., Phenom.*, 2007, **25**, 2558–2561.
90 C. Cao, M. Daly, B. Chen, J. Y. Howe, C. V. Singh, T. Filleter and Y. Sun, *Nano Lett.*, 2015, **15**, 6528–6534.
91 C. Rong, T. Su, Z. Li, T. Chu, M. Zhu, Y. Yan, B. Zhang and F.-Z. Xuan, *Nat. Commun.*, 2024, **15**, 1566.
92 A. Lipatov, M. Alhabeb, H. Lu, S. Zhao, M. J. Loes, N. S. Vorobeva, Y. Dall'Agnese, Y. Gao, A. Gruverman, Y. Gogotsi and A. Sinitskii, *Adv. Electron. Mater.*, 2020, **6**, 1901382.
93 K. Liu, Q. Yan, M. Chen, W. Fan, Y. Sun, J. Suh, D. Fu, S. Lee, J. Zhou, S. Tongay, J. Ji, J. B. Neaton and J. Wu, *Nano Lett.*, 2014, **14**, 5097–5103.
94 A. Castellanos-Gomez, M. Poot, G. A. Steele, H. S. Van Der Zant, N. Agraït and G. Rubio-Bollinger, *Adv. Mater.*, 2012, **24**, 772–775.
95 A. Castellanos-Gomez, M. Poot, G. A. Steele, H. S. Van der Zant, N. Agraït and G. Rubio-Bollinger, *Nanoscale Res. Lett.*, 2012, **7**, 1–4.
96 Y. Yang, Z. Song, G. Lu, Q. Zhang, B. Zhang, B. Ni, C. Wang, X. Li, L. Gu, X. Xie, H. Gao and J. Lou, *Nature*, 2021, **594**, 57–61.
97 S. M. Kim, A. Hsu, M. H. Park, S. H. Chae, S. J. Yun, J. S. Lee, D.-H. Cho, W. Fang, C. Lee, T. Palacios, M. Dresselhaus, K. K. Kim, Y. H. Lee and J. Kong, *Nat. Commun.*, 2015, **6**, 8662.
98 L. Song, L. Ci, H. Lu, P. B. Sorokin, C. Jin, J. Ni, A. G. Kvashnin, D. G. Kvashnin, J. Lou and B. I. Yakobson, *Nano Lett.*, 2010, **10**, 3209–3215.

99 R. Zhang, V. Koutsos and R. Cheung, *Appl. Phys. Lett.*, 2016, **108**, 042104.
100 A. Falin, M. Holwill, H. Lv, W. Gan, J. Cheng, R. Zhang, D. Qian, M. R. Barnett, E. J. G. Santos, K. S. Novoselov, T. Tao, X. Wu and L. H. Li, *ACS Nano*, 2021, **15**, 2600–2610.
101 H. Yan, C. Vajner, M. Kuhlman, L. Guo, L. Li, P. T. Araujo and H.-T. Wang, *Appl. Phys. Lett.*, 2016, **109**, 032103.
102 L. Guo, H. Yan, Q. Moore, M. Buettner, J. Song, L. Li, P. T. Araujo and H.-T. J. N. Wang, *Nanoscale*, 2015, **7**, 11915–11921.
103 J.-W. Jiang and H. S. Park, *J. Phys. D: Appl. Phys.*, 2014, **47**, 385304.
104 A. Castellanos-Gomez, M. Poot, A. Amor-Amorós, G. A. Steele, H. S. van der Zant, N. Agraït and G. J. N. R. Rubio-Bollinger, *Nano Res.*, 2012, **5**, 550–557.
105 W. Qian, H. Fu, Y. Sun, Z. Wang, H. Wu, Z. Kou, B.-W. Li, D. He and C.-W. Nan, *Adv. Mater.*, 2022, **34**, 2206101.
106 S. Luo, S. Patole, S. Anwer, B. Li, T. Delclos, O. Gogotsi, V. Zahorodna, V. Balitskyi and K. Liao, *Nanotechnology*, 2020, **31**, 395704.
107 H. Chen, M. B. Müller, K. J. Gilmore, G. G. Wallace and D. Li, *Adv. Mater.*, 2008, **20**, 3557–3561.
108 Y. Li, T. Yang, T. Yu, L. Zheng and K. Liao, *J. Mater. Chem.*, 2011, **21**, 10844–10851.
109 D. A. Dikin, S. Stankovich, E. J. Zimney, R. D. Piner, G. H. B. Dommett, G. Evmenenko, S. T. Nguyen and R. S. Ruoff, *Nature*, 2007, **448**, 457–460.
110 A. Liu, X. Zhang, Z. Liu, Y. Li, X. Peng, X. Li, Y. Qin, C. Hu, Y. Qiu, H. Jiang, Y. Wang, Y. Li, J. Tang, J. Liu, H. Guo, T. Deng, S. Peng, H. Tian and T.-L. Ren, *Nano-Micro Lett.*, 2024, **16**, 119.
111 W. Yu, L. Sisi, Y. Haiyan and L. Jie, *RSC Adv.*, 2020, **10**, 15328–15345.
112 L. David and G. J. T. J. o P. C. C. Singh, *J. Phys. Chem. C*, 2014, **118**, 28401–28408.
113 B. Anasori, Y. Xie, M. Beidaghi, J. Lu, B. C. Hosler, L. Hultman, P. R. C. Kent, Y. Gogotsi and M. W. Barsoum, *ACS Nano*, 2015, **9**, 9507–9516.
114 B. Anasori and Y. Gogotsi, *Graphene 2D Nanomater.*, 2022, **7**, 75–79.
115 M. Naguib, M. Kurtoglu, V. Presser, J. Lu, J. Niu, M. Heon, L. Hultman, Y. Gogotsi and M. W. Barsoum, *Adv. Mater.*, 2011, **23**, 4248–4253.
116 M. Downes, C. E. Shuck, R. W. Lord, M. Anayee, M. Shekhirev, R. J. Wang, T. Hryhorchuk, M. Dahlqvist, J. Rosen and Y. Gogotsi, *ACS Nano*, 2023, **17**, 17158–17168.
117 Y. Gogotsi, *Chem. Mater.*, 2023, **35**, 8767–8770.
118 A. Lee, M. Shekhirev, M. Anayee and Y. Gogotsi, *Graphene 2D Mater.*, 2024, **9**, 77–85.
119 T. S. Mathis, K. Maleski, A. Goad, A. Sarycheva, M. Anayee, A. C. Foucher, K. Hantanasirisakul, C. E. Shuck, E. A. Stach and Y. Gogotsi, *ACS Nano*, 2021, **15**, 6420–6429.
120 S. Vorotilo, C. E. Shuck, M. Anayee, M. Shekhirev, K. Matthews, R. W. Lord, I. Roslyk, V. Balitskiy, V. Zahorodna and O. Gogotsi, *Graphene 2D Mater.*, 2023, **8**, 93–105.
121 A. Thakur, N. Chandran, K. Davidson, A. Bedford, H. Fang, Y. Im, V. Kanduri, B. C. Wyatt, S. K. Nemani, V. Poliukhova, R. Kumar, Z. Fakhraai and B. Anasori, *Small Methods*, 2023, **7**, 2300030.
122 S. Park, J. W. Suk, J. An, J. Oh, S. Lee, W. Lee, J. R. Potts, J.-H. Byun and R. S. Ruoff, *Carbon*, 2012, **50**, 4573–4578.
123 T. Zhou, C. Wu, Y. Wang, A. P. Tomsia, M. Li, E. Saiz, S. Fang, R. H. Baughman, L. Jiang and Q. Cheng, *Nat. Commun.*, 2020, **11**, 2077.
124 J. Yang, M. Li, S. Fang, Y. Wang, H. He, C. Wang, Z. Zhang, B. Yuan, L. Jiang, R. H. Baughman and Q. Cheng, *Science*, 2024, **383**, 771–777.
125 J. Zhong, W. Sun, Q. Wei, X. Qian, H.-M. Cheng and W. Ren, *Nat. Commun.*, 2018, **9**, 3484.
126 G. Xin, H. Sun, T. Hu, H. R. Fard, X. Sun, N. Koratkar, T. Borca-Tasciuc and J. Lian, *Adv. Mater.*, 2014, **26**, 4521–4526.
127 S. Liu, K. Hu, M. Cerruti and F. Barthelat, *Carbon*, 2020, **158**, 426–434.
128 M. Chen, Q. Wang, M. Trubyanov, K. Yang, A. S. Aglikov, G. Qi, E. V. Skorb, K. S. Novoselov and D. V. Andreeva, *Mater. Des.*, 2023, **233**, 112205.
129 L. Peng, Z. Xu, Z. Liu, Y. Guo, P. Li and C. Gao, *Adv. Mater.*, 2017, **29**, 1700589.
130 X. Zhang, Y. Guo, Y. Liu, Z. Li, W. Fang, L. Peng, J. Zhou, Z. Xu and C. Gao, *Carbon*, 2020, **167**, 249–255.
131 X. Chen, X. Deng, N. Y. Kim, Y. Wang, Y. Huang, L. Peng, M. Huang, X. Zhang, X. Chen, D. Luo, B. Wang, X. Wu, Y. Ma, Z. Lee and R. S. Ruoff, *Carbon*, 2018, **132**, 294–303.
132 Z. Zhuang, H. Chen and C. Li, *ACS Nano*, 2023, **17**, 10628–10636.
133 K. W. Putz, O. C. Compton, M. J. Palmeri, S. T. Nguyen and L. C. J. A. F. M. Brinson, *Adv. Funct. Mater.*, 2010, **20**, 3322–3329.
134 S. Park, K.-S. Lee, G. Bozoklu, W. Cai, S. T. Nguyen and R. S. Ruoff, *ACS Nano*, 2008, **2**, 572–578.
135 L. Liu, Y. Gao, Q. Liu, J. Kuang, D. Zhou, S. Ju, B. Han and Z. Zhang, *Small*, 2013, **9**, 2466–2472.
136 Y. Gao, L.-Q. Liu, S.-Z. Zu, K. Peng, D. Zhou, B.-H. Han and Z. Zhang, *ACS Nano*, 2011, **5**, 2134–2141.
137 Z. Liu, W. Wang, J. Tan, J. Liu, M. Zhu, B. Zhu and Q. Zhang, *J. Mater. Chem. C*, 2020, **8**, 7170–7180.
138 J. Zhou, D. Shi, Y. Wang, M. Chen and W. J. M. R. B. Dong, *Mater. Res. Bull.*, 2022, **154**, 111939.
139 C. Cai, W. Zhou and Y. J. C. E. J. Fu, *Chem. Eng. J.*, 2021, **418**, 129275.
140 G. S. Lee, T. Yun, H. Kim, I. H. Kim, J. Choi, S. H. Lee, H. J. Lee, H. S. Hwang, J. G. Kim, D. W. Kim, H. M. Lee, C. M. Koo and S. O. Kim, *ACS Nano*, 2020, **14**, 11722–11732.
141 J. Cao, Z. Zhou, Q. Song, K. Chen, G. Su, T. Zhou, Z. Zheng, C. Lu and X. Zhang, *ACS Nano*, 2020, **14**, 7055–7065.
142 W. Li, T. Zhou, Z. Zhang, L. Li, W. Lian, Y. Wang, J. Lu, J. Yan, H. Wang, L. Wei and Q. Cheng, *Science*, 2024, **385**, 62–68.
143 J. Zhang, N. Kong, S. Uzun, A. Levitt, S. Seyedin, P. A. Lynch, S. Qin, M. Han, W. Yang, J. Liu, X. Wang, Y. Gogotsi and J. M. Razal, *Adv. Mater.*, 2020, **32**, 2001093.

144 S. Wan, X. Li, Y. Chen, N. Liu, S. Wang, Y. Du, Z. Xu, X. Deng, S. Dou and L. J. N. C. Jiang, *Nat. Commun.*, 2022, **13**, 7340.
145 R. Chen, H. Tang, Y. Dai, W. Zong, W. Zhang, G. He and X. Wang, *ACS Nano*, 2022, **16**, 19124–19132.
146 X. Zhao, Z. Wang, J. Dong, T. Huang, Q. Zhang and L. Zhang, *J. Power Sources*, 2020, **470**, 228356.
147 J. Liu, Z. Liu, H.-B. Zhang, W. Chen, Z. Zhao, Q.-W. Wang and Z.-Z. Yu, *Adv. Electron. Mater.*, 2020, **6**, 1901094.
148 Q. Liu, Y. Zhang, Y. Liu, Z. Liu, B. Zhang and Q. Zhang, *J. Alloys Compd.*, 2021, **860**, 158151.
149 E. Gao, Y. Wen, Y. Yuan, C. Li and Z. Xu, *Carbon*, 2017, **118**, 467–474.
150 S. E. Taher, J. M. Ashraf, K. Liao and R. K. Abu Al-Rub, *Graphene 2D Mater.*, 2023, **8**, 161–178.
151 J. Fu, S. E. Taher, R. K. Abu Al-Rub, T. Zhang, V. Chan and K. Liao, *Adv. Eng. Mater.*, 2022, **24**, 2101388.
152 W. Yang, J. Yang, J. J. Byun, F. P. Moissinac, J. Xu, S. J. Haigh, M. Domingos, M. A. Bissett, R. A. W. Dryfe and S. Barg, *Adv. Mater.*, 2019, **31**, 1902725.
153 Z. Wang, N. Zhang, M. Yu, J. Liu, S. Wang and J. Qiu, *J. Energy Chem.*, 2019, **37**, 183–191.
154 M. Ghidiu, M. R. Lukatskaya, M.-Q. Zhao, Y. Gogotsi and M. W. Barsoum, *Nature*, 2014, **516**, 78–81.
155 A. D. Dillon, M. J. Ghidiu, A. L. Krick, J. Griggs, S. J. May, Y. Gogotsi, M. W. Barsoum and A. T. Fafarman, *Adv. Funct. Mater.*, 2016, **26**, 4162–4168.
156 K. Hantanasirisakul, M.-Q. Zhao, P. Urbankowski, J. Halim, B. Anasori, S. Kota, C. E. Ren, M. W. Barsoum and Y. Gogotsi, *Adv. Electron. Mater.*, 2016, **2**, 1600050.
157 S. Casaluci, M. Gemmi, V. Pellegrini, A. Di Carlo and F. Bonaccorso, *Nanoscale*, 2016, **8**, 5368–5378.
158 M. Alhabeb, K. Maleski, B. Anasori, P. Lelyukh, L. Clark, S. Sin and Y. Gogotsi, *Chem. Mater.*, 2017, **29**, 7633–7644.
159 A. Lipatov, M. Alhabeb, M. R. Lukatskaya, A. Boson, Y. Gogotsi and A. Sinitskii, *Adv. Electron. Mater.*, 2016, **2**, 1600255.
160 Z. Ling, C. E. Ren, M.-Q. Zhao, J. Yang, J. M. Giammarco, J. Qiu, M. W. Barsoum and Y. Gogotsi, *Proc. Natl. Acad. Sci. U. S. A.*, 2014, **111**, 16676–16681.
161 M. Wang, S. K. Jang, W.-J. Jang, M. Kim, S.-Y. Park, S.-W. Kim, S.-J. Kahng, J.-Y. Choi, R. S. Ruoff, Y. J. Song and S. Lee, *Adv. Mater.*, 2013, **25**, 2746–2752.
162 D. Wang, C. Zhou, A. S. Filatov, W. Cho, F. Lagunas, M. Wang, S. Vaikuntanathan, C. Liu, R. F. Klie and D. V. Talapin, *Science*, 2023, **379**, 1242–1247.
163 Y. Wu, S. Wang and K. Komvopoulos, *J. Mater. Res.*, 2020, **35**, 76–89.
164 J. Wang, J. He, D. Kan, K. Chen, M. Song and W. Huo, *Crystals*, 2022, **12**, 1034.
165 Y. Liu, P. Li, F. Wang, W. Fang, Z. Xu, W. Gao and C. Gao, *Carbon*, 2019, **155**, 462–468.
166 D. Jiang, J. Zhang, S. Qin, Z. Wang, K. A. S. Usman, D. Hegh, J. Liu, W. Lei and J. M. Razal, *ACS Nano*, 2021, **15**, 5000–5010.
167 G. Shao, D. A. H. Hanaor, X. Shen and A. Gurlo, *Adv. Mater.*, 2020, **32**, 1907176.
168 A. E. Garcia, C. S. Wang, R. N. Sanderson, K. M. McDevitt, Y. Zhang, L. Valdevit, D. R. Mumm, A. Mohraz and R. Ragan, *Nanoscale Adv.*, 2019, **1**, 3870–3882.
169 K. Nakanishi, D. Labonte, T. Cebo, V. P. Veigang-Radulescu, Y. Fan, B. Brennan, A. J. Pollard, S. Hofmann and N. A. Fleck, *Acta Mater.*, 2020, **201**, 254–265.
170 J. Patenaude, B. C. Wyatt, S. K. Nemani and B. Anasori, *MRS Adv.*, 2024, **9**, 551–556.
171 O. C. Compton, S. W. Cranford, K. W. Putz, Z. An, L. C. Brinson, M. J. Buehler and S. T. Nguyen, *ACS Nano*, 2012, **6**, 2008–2019.
172 N. V. Medhekar, A. Ramasubramaniam, R. S. Ruoff and V. B. Shenoy, *ACS Nano*, 2010, **4**, 2300–2306.
173 S. Lin, S. Ju, J. Zhang, G. Shi, Y. He and D. Jiang, *RSC Adv.*, 2019, **9**, 1419–1427.
174 K. Hantanasirisakul, T. Chantaurai, A. Limsukhon, P. Chomkhuntod, P. Poprom and M. Sawangphruk, *Adv. Mater. Interfaces*, 2022, **9**, 2201457.
175 J. D. Renteria, S. Ramirez, H. Malekpour, B. Alonso, A. Centeno, A. Zurutuza, A. I. Cocemasov, D. L. Nika and A. A. Balandin, *Adv. Funct. Mater.*, 2015, **25**, 4664–4672.
176 F. A. Chowdhury, T. Morisaki, J. Otsuki and M. Sahabul Alam, *Appl. Nanosci.*, 2013, **3**, 477–483.
177 H. Tang, R. Wang, L. Shi, E. Sheremet, R. D. Rodriguez and J. Sun, *Chem. Eng. J.*, 2021, **425**, 131472.
178 C.-M. Chen, J.-Q. Huang, Q. Zhang, W.-Z. Gong, Q.-H. Yang, M.-Z. Wang and Y.-G. Yang, *Carbon*, 2012, **50**, 659–667.
179 G. G. Jernigan, J. A. Nolde, N. A. Mahadik, E. R. Cleveland, J. E. Boercker, M. B. Katz, J. T. Robinson and E. H. Aifer, *J. Appl. Phys.*, 2017, **122**, 075301.
180 P. Cazón, G. Velázquez and M. Vázquez, *Food Hydrocolloids*, 2020, **103**, 105657.
181 N.-j Song, C.-x Lu, C.-m Chen, C.-l Ma and Q.-q Kong, *New Carbon Mater.*, 2017, **32**, 221–226.
182 D.-T. Phan and G.-S. Chung, *Sens. Actuators, B*, 2015, **220**, 1050–1055.
183 O. C. Compton and S. T. Nguyen, *Small*, 2010, **6**, 711–723.
184 E. P. Simonenko, I. A. Nagornov, A. S. Mokrushin, A. A. Averin, Y. M. Gorban, T. L. Simonenko, N. P. Simonenko and N. T. Kuznetsov, *Micromachines*, 2023, **14**, 725.
185 K. Ma, Y. Dong, H. Jiang, Y. Hu, P. Saha and C. Li, *Chem. Eng. J.*, 2021, **413**, 127479.
186 B. Xia, Z. Wang, T. Wang, S. Chen, H. Wu, B. Zhang, Y. Si, Z. Chen, B.-W. Li, Z. Kou and D. He, *iScience*, 2022, **25**, 105001.
187 Z. Xing, Y. Si, H. Jin, B. Zhang, Z. Chen, J. Fang, J. Zhang, C. Chen and D. He, *Adv. Mater. Technol.*, 2024, **9**, 2302098.
188 Z. Fan, Y. Yang, H. Ma, Y. Wang, Z. Xie and Y. Liu, *Carbon*, 2022, **186**, 150–159.
189 S. Wan, X. Li, Y. Chen, N. Liu, Y. Du, S. Dou, L. Jiang and Q. Cheng, *Science*, 2021, **374**, 96–99.
190 A. K. Grebenko, G. Drozdov, Y. G. Gladush, I. Ostanin, S. S. Zhukov, A. V. Melentyev, E. M. Khabushev, A. P. Tsapenko, D. V. Krasnikov, B. Afinogenov, A. G. Temiryazev, V. V. Dremov, T. Dumitricã, M. Li, H. Hijazi, V. Podzorov, L. C. Feldman and A. G. Nasibulin, *Carbon*, 2022, **196**, 979–987.

191 J. Zhu, F. Li, Y. Hou, H. Li, D. Xu, J. Tan, J. Du, S. Wang, Z. Liu, H. Wu, F. Wang, Y. Su and H.-M. Cheng, *Nat. Mater.*, 2024, **23**, 604–611.
192 F. Xu, R. Chen, Z. Lin, X. Sun, S. Wang, W. Yin, Q. Peng, Y. Li and X. He, *J. Mater. Chem. C*, 2018, **6**, 12321–12328.
193 D. Pradhan, S. P. Ghosh, A. Gartia, K. K. Sahoo, G. Bose and J. P. Kar, *Superlattices Microstruct.*, 2020, **145**, 106598.
194 J. S. Park, S. M. Cho, W.-J. Kim, J. Park and P. J. Yoo, *ACS Appl. Mater. Interfaces*, 2011, **3**, 360–368.
195 C. Teng, D. Xie, J. Wang, Z. Yang, G. Ren and Y. Zhu, *Adv. Funct. Mater.*, 2017, **27**, 1700240.
196 J. Zhao, S. Zeng, B. Wu, S.-L. Zhang and Z.-B. Zhang, *Diamond Relat. Mater.*, 2018, **84**, 141–145.
197 W. Yang, H. Bai, B. Jiang, C. Wang, W. Ye, Z. Li, C. Xu, X. Wang and Y. Li, *Nano Res.*, 2022, **15**, 9926–9935.
198 J. Wang, D. Jiang, M. Zhang, Y. Sun, M. Jiang, Y. Du and J. Liu, *J. Mater. Chem. A*, 2023, **11**, 1419–1429.
199 J. Zhang, L. zhang, C. Lv, L. Gao, X. Chen, S. Luo, Y. Chen, Y. Ren, L. Chang, W. Guo and Q. Tang, *Ind. Crops Prod.*, 2024, **216**, 118700.
200 X. Huang, J. Huang, G. Zhou, Y. Wei, P. Wu, A. Dong and D. Yang, *Small*, 2022, **18**, 2200829.
201 R. Yang, L. Mei, Z. Lin, Y. Fan, J. Lim, J. Guo, Y. Liu, H. S. Shin, D. Voiry, Q. Lu, J. Li and Z. Zeng, *Nat. Rev. Chem.*, 2024, **8**, 410–432.
202 M. Lounasvuori, T. Zhang, Y. Gogotsi and T. Petit, *J. Phys. Chem. C*, 2024, **128**, 2803–2813.
203 A. Seko, S. Sakaida, M. Koyanagi, Y. Okada, T. Torita, M. Anayee, M. Shekhirev and Y. Gogotsi, *MRS Commun.*, 2023, **13**, 812–817.
204 H. Chen, Y. Wen, Y. Qi, Q. Zhao, L. Qu and C. Li, *Adv. Funct. Mater.*, 2020, **30**, 1906996.
205 L. David, R. Bhandavat and G. Singh, *ACS Nano*, 2014, **8**, 1759–1770.
206 Z. Yang, Y. Huang, F. Ma, Y. Sun, K. Xu and P. K. Chu, *Eur. Phys. J. B*, 2015, **88**, 1–8.
207 T. Han, Y. Luo and C. Wang, *J. Phys. D: Appl. Phys.*, 2014, **47**, 025303.
208 Z.-D. Sha, Q.-X. Pei, K. Zhou, Z. Dong and Y.-W. J. E. M. L. Zhang, *Extreme Mech. Lett.*, 2018, **19**, 39–45.
209 Y. Chen, H. Xiao, Y. Liu and X. Chen, *J. Phys. Chem. C*, 2018, **122**, 6368–6378.
210 Q.-X. Pei, Z.-D. Sha, Y.-Y. Zhang and Y.-W. Zhang, *J. Appl. Phys.*, 2014, **115**, 023519.
211 M. M. Billah, M. S. Rabbi, K. A. Rahman and P. Acar, *Mater. Chem. Phys.*, 2024, **312**, 128581.
212 M. M. Hassan, J. Islam, W. R. Sajal, M. A.-A. B. Shuvo and S. Goni, *Mater. Today Commun.*, 2023, **37**, 106898.
213 S. Vinod, C. S. Tiwary, L. D. Machado, S. Ozden, J. Cho, P. Shaw, R. Vajtai, D. S. Galvão and P. M. Ajayan, *Nano Lett.*, 2016, **16**, 1127–1131.

